ADVANCED ELECTRONIC MATERIALS
Open Access
www.advelectronicmat.de

Trap-Assisted Memristive Switching in HfO_2-Based Devices Studied by In Situ Soft and Hard X-Ray Photoelectron Spectroscopy

Finn Zahari, Richard Marquardt, Matthias Kalläne, Ole Gronenberg, Christoph Schlueter, Yury Matveyev, Georg Haberfehlner, Florian Diekmann, Alena Nierhauve, Jens Buck, Arndt Hanff, Gitanjali Kolhatkar, Gerald Kothleitner, Lorenz Kienle, Martin Ziegler, Jürgen Carstensen, Kai Rossnagel, and Hermann Kohlstedt**

Memristive devices are under intense development as non-volatile memory elements for extending the computing capabilities of traditional silicon technology by enabling novel computing primitives. In this respect, interface-based memristive devices are promising candidates to emulate synaptic functionalities in neuromorphic circuits aiming to replicate the information processing of nervous systems. A device composed of Nb/NbO_x/Al_2O_3/HfO_2/Au that shows promising features like analog switching, no electro-forming, and high current-voltage non-linearity is reported. Synchrotron-based X-ray photoelectron spectroscopy and depth-dependent hard X-ray photoelectron spectroscopy are used to probe in situ different resistance states and thus the origin of memristive switching. Spectroscopic evidence for memristive switching based on the charge state of electron traps within HfO_2 is found. Electron energy loss spectroscopy and transmission electron microscopy support the analysis. A device model is proposed that considers a two-terminal metal–insulator–semiconductor structure in which traps within the insulator (HfO_2/Al_2O_3) modulate the space charge region within the semiconductor (NbO_x) and, thereby, the overall resistance. The experimental findings are in line with impedance spectroscopy data reported in the companion paper (Marquardt et al). Both works complement one another to derive a detailed device model, which helps to engineer device performance and integrate devices into silicon technology.

1. Introduction

Today's digital computers are based on a separation of memory and computation. Thus, data has to be continually transferred from the memory location to the location of computing and vice versa in traditional computing architecture, leading to high latency and energy consumption.[1–3] One potential concept to overcome this so-called von Neumann bottleneck for certain applications is the development of neuromorphic computing architectures, which aim to emulate information processing in the human brain.[4–7] In biology, information processing takes place in huge networks of neurons and synapses, without physical separation between computation and memory,[8] leading to an impressive performance in tasks like sensory processing, motor control, and pattern recognition,[9] while at the same time consuming less energy, orders of magnitude lower than digital computers require to conduct similar tasks.[5,6,10,11]

F. Zahari, R. Marquardt, H. Kohlstedt
Nanoelectronics
Faculty of Engineering
Kiel University
24143 Kiel, Germany
E-mail: fnz@tf.uni-kiel.de; hko@tf.uni-kiel.de

The ORCID identification number(s) for the author(s) of this article can be found under https://doi.org/10.1002/aelm.202201226.

DOI: 10.1002/aelm.202201226

M. Kalläne, F. Diekmann, A. Nierhauve, J. Buck, A. Hanff, K. Rossnagel
Institute of Experimental and Applied Physics
Kiel University
24098 Kiel, Germany

M. Kalläne, F. Diekmann, A. Hanff, K. Rossnagel
Ruprecht Haensel Laboratory
Kiel University
24098 Kiel, Germany

M. Kalläne, L. Kienle, K. Rossnagel, H. Kohlstedt
Kiel Nano Surface and Interface Science KiNSIS
Kiel University
24118 Kiel, Germany

O. Gronenberg, L. Kienle
Synthesis and Real Structure
Faculty of Engineering, Kiel University
24143 Kiel, Germany

ADVANCED ELECTRONIC MATERIALS
Open Access
www.advelectronicmat.de

Memristive devices are widely investigated as a key element for neuromorphic computing,[3,10–13] and hybrid memristive-complementary metal-oxide–semiconductor (CMOS) circuits are examined to extend performance and reduce the energy consumption of traditional CMOS technology.[9,14] Among other applications, memristive devices can be exploited to emulate functionalities of biological synapses, such as long-term potentiation (LTP), long-term depression (LTD), spike-timing-dependent plasticity (STDP), and paired-pulse facilitation (PPF).[11,15–22] Memristive devices are often composed of a metal–insulator–metal (MIM) structure in which the resistance can be varied by electrical stimuli, allowing them to be used as non-volatile memory elements.[5,13,23,24] Many different physical mechanisms leading to memristive behavior have been reported so far.[5,13,24–26] Among them, devices based on a Schottky barrier height or width modulation[22,27–36] are interesting candidates for neuromorphic circuits.[11,25] These interface-based memristive devices show gradual, that is, analog switching, and do not require initial electro-forming.[7,13,25] Moreover, arranging memristive devices in passive crossbar arrays for dense device integration requires selector devices to prevent parasitic current flows when a specific device is addressed,[3,10,11] as recently reviewed in ref. [37]. Various kinds of selector devices, such as transistors[38,39] or volatile memristive devices,[40] can serve as selector elements when connected in series with the non-volatile memristive devices. In this respect, the high current–voltage (I–V) non-linearity of interface-type memristive devices allows passive crossbar integration[29,41,42] without additional selector elements.[3,10,11,37] Switching processes are reported to be caused by a rearrangement of ions or vacancies[22,29,31–33,35] or by the charging and discharging of electron traps.[27,28,30,34,36,43] However, spectroscopic evidence for the proposed switching mechanism is often missing.

Among a multitude of different methods to probe memristive switching,[44] transmission electron microscopy (TEM) together with energy electron loss spectroscopy (EELS),[45] and photoelectron spectroscopy (PES)[46] are widely used techniques to study structural, chemical and electronic properties of the material systems. In particular, X-ray photoelectron spectroscopy (XPS)[46] and hard X-ray photoelectron spectroscopy (HAXPES)[47] allow to probe film compositions, chemical states, band alignment as well as band bending in buried layers and their dependence on depth.[46,48,49] Hard X-rays (>2 keV) from synchrotron sources with orders of magnitude higher photon flux compared to laboratory sources provide an information depth of up to a few 10 nm while simultaneously allowing for reasonable energy resolution.[47] Furthermore, non-destructive depth profiling is possible with XPS/HAXPES by collecting photoelectrons that are ejected with different angles of emission.[46,47] Thus, XPS and HAXPES allow in situ and in operando investigations of memristive switching processes[50–55] in functional devices, where switching takes place within a few 10 nm below the sample surface.

Memristive devices based on metal oxides are often composed of oxide bi- or multi-layers sandwiched between two metal electrodes.[22,33,42,43,55–62] One oxide serves as an active switching material, while the other oxides act, for example, as diffusion barriers,[33,57,62] as oxygen ion reservoirs,[22,55,59] as rectification layers,[43,56,60,61,63] or affect the local heat distribution,[59] thus significantly improving the device characteristics. Within this work, an analog switching interface-type memristive device consisting of the layer sequence $Nb/NbO_x/Al_2O_3/HfO_2/Au$ (see **Figure 1**) is investigated. HfO_2 is widely investigated and applied as an active switching layer in memristive devices[22,38,39,42,50–56,62,63] due to its CMOS compatibility.[64] Among other applications, hafnia is used as a gate dielectric for metal-oxide–semiconductor field-effect transistors (MOSFETs),[64,65] as charge trapping layer in charge trap flash (CTF) memory,[66] and as an active layer in CMOS-integrated filamentary-type resistive random access memory (RRAM) devices.[38,39] On the other hand, Al_2O_3 is reported to serve as a diffusion barrier for oxygen ions[33,57,58,62] which can lead to an enhanced retention time of interface-type memristive devices, and simultaneously suppress an oxygen exchange with adjacent layers.[33] Alumina is also compatible with CMOS technology.[62] Furthermore, stoichiometric Nb_2O_5 is known to be a good insulator,[67] but oxygen-deficient films are reported to show n-type semiconducting behavior.[67,68] Thus, a NbO_x layer can in principle be used to fabricate rectifying metal–semiconductor (MS) or metal–insulator–semiconductor (MIS) devices.[69,70] The investigated $Nb/NbO_x/Al_2O_3/HfO_2/Au$ device is based on similar devices with a NbO_y layer instead of HfO_2.[33] The Schottky barrier of the NbO_y/Au interface was reported to be altered by the drift of negatively charged oxygen ions, while the probability for tunneling through the Al_2O_3 is simultaneously affected,[33] as modeled by a kinetic Monte Carlo simulation,[71] and a cloud-in-a-cell (CIC) scheme[72] that also covers the device variability. Furthermore, the charging and discharging of interface trap states are also reported as a possible mechanism responsible for memristive switching.[33] The integration into passive crossbar

C. Schlueter, Y. Matveyev
Deutsches Elektronen-Synchrotron DESY
22607 Hamburg, Germany

G. Haberfehlner, G. Kothleitner
Institute of Electron Microscopy and Nanoanalysis
Graz University of Technology
Graz 8010, Austria

A. Nierhauve, J. Buck, K. Rossnagel
Ruprecht Haensel Laboratory
Deutsches Elektronen-Synchrotron DESY
22607 Hamburg, Germany

G. Kolhatkar
Department of Engineering Physics
McMaster University, Hamilton
Ontario L8S 4L7, Canada

G. Kothleitner
Graz Centre for Electron Microscopy
Graz 8010, Austria

M. Ziegler
Department of Electrical Engineering and Information Technology
Technische Universtität Ilmenau
98693 Ilmenau, Germany

M. Ziegler
Institute of Micro and Nanotechnologies MacroNano
Technische Universtität Ilmenau
98693 Ilmenau, Germany

J. Carstensen
Functional Nanomaterials
Faculty of Engineering
Kiel University
24143 Kiel, Germany

ADVANCED ELECTRONIC MATERIALS
Open Access
www.advelectronicmat.de

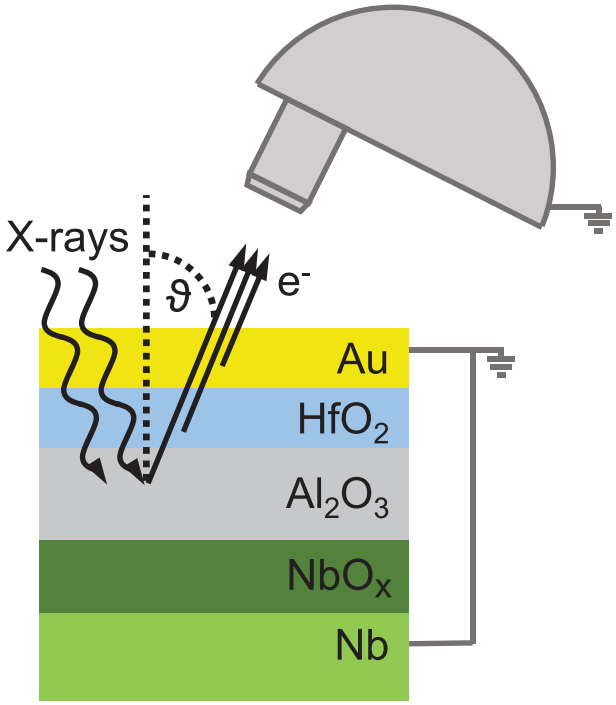

Figure 1. Schematic illustration of the HAXPES measurement setup and the probed devices: An X-ray beam is directed onto the sample surface. The kinetic energies of electrons ejected at specific polar angles of emission ϑ are measured. During HAXPES measurements, the device electrodes are connected to common ground with the analyzer to ensure charge compensation and to obtain defined electrostatic conditions within the device. The memristive state can be read out and switched in the vacuum chamber by connecting a source measurement unit to the electrodes. When voltages were applied, the beam was never directed onto the sample.

arrays[41] and the utilization as artificial synapses in neuromorphic networks for pattern recognition tasks have already been reported for the devices based on NbO_y as the active layer.[19,41]

Here, the origin of memristive switching in the HfO_2-based devices is investigated by depth-dependent synchrotron-based HAXPES and synchrotron-based XPS with soft X-rays. Varying the recorded angle of emission ϑ allowed for non-destructive depth profiling of chemical and electronic properties. The measurement setup is schematically illustrated in Figure 1. In combination with structural data from TEM, chemical information from EELS, and current density versus voltage (J–V) characterizations, a model to qualitatively describe the physics of the interface-based memristive device is proposed in this manuscript: A two-terminal MIS structure, in which electron traps within the insulator modulate the space-charge region within the semiconductor and, thereby, the Schottky barrier height, is consistently used to explain the findings from all experiments. In particular, we identify a causal relationship between the charge-trapping state of HfO_2 and the overall device resistance. Spectroscopic evidence (by XPS/HAXPES) for such a switching mechanism has not been reported so far. Furthermore, impedance spectroscopy (ImpSpec)[73] is exploited by Marquardt et al. in a companion paper[74] to probe memristive switching in the same device. The findings presented in both papers indicate that the memristive switching can be attributed to a Schottky barrier modulation by a charge-trapping mechanism. The obtained device model is advantageous for both device integration into silicon technology to exploit the benefits of hybrid memristive-CMOS neuromorphic circuits and engineering of device characteristics for specific applications. In this respect, some design rules for CMOS integration are provided at the end of this work.

2. Results

2.1. Electrical Characterization

Typical semi-logarithmic current density versus voltage ($|J|$–V) characteristics of devices from the reference wafer (see Experimental Section for fabrication and characterization details) with a top electrode size of 625 μm^2 are presented in **Figure 2**a. Here, the mean behavior of ten adjacent devices is depicted in black, while the characteristics of single devices are drawn in gray. The inset of Figure 2a shows the mean $|J|$–V characteristics for low applied voltages (±1.2 V). The hysteresis observed for small current densities arises from capacitive effects of the measurement setup since only noise is detected and no memristive switching takes place. As it is shown in Figure 2a, higher voltages (± 3.7 V) induce memristive switching. The diode-like electrical properties allow for integration into passive crossbar arrays without requiring additional selector devices.[41] Furthermore, no initial electro-forming or current compliance is needed to operate the devices and the observed smooth hysteresis reveals analog switching. Such analog interface-type memristive devices can be used for emulating synaptic functionalities, as reported for various devices.[15,17,19,22,42] In particular, devices with a similar material stack produced with the very same processes but containing a sputtered NbO_y layer instead of HfO_2[33] show similar electrical characteristics. The possibility of using these NbO_y-based devices for the emulation of synaptic functionalities has been shown experimentally on both the device level[18,19] and the network level.[41]

The area-dependent current transport is shown in Figure 2b. Here, the resistance mean value and standard deviation of ten neighboring devices per area for a bias voltage of 1.2 V are depicted. The resistance scales linearly with the area of the device in the high resistance state (HRS) and in a low resistance state (LRS). Thus, homogeneous current transport through the whole device area is indicated for both HRS and LRS.

The relaxation of the LRS toward higher resistances is shown in Figure 2c as red circles. The device is set to an LRS by applying a positive voltage sweep with V_{max} = 3.7 V and the device resistance R is read out with 0.5 V voltage pulses of 4 s length after the set sweep, and with delay times of 300 (next 12 pulses), and 1800 s (all further pulses). R is further divided by the initial resistance R_0, which is determined as the mean of ten consecutive read out pulses prior to switch the device. The resistance increases with time so that it approaches R_0 in ≈25.5 h and does not increase further in the next 13 h. The relaxation process can be fitted with a power law of the form $\propto t^{\alpha}$, as reported for other memristive devices,[22,30,33,34] as well as for describing charge trapping under bias in HfO_2.[75] In

ADVANCED ELECTRONIC MATERIALS
Open Access
www.advelectronicmat.de

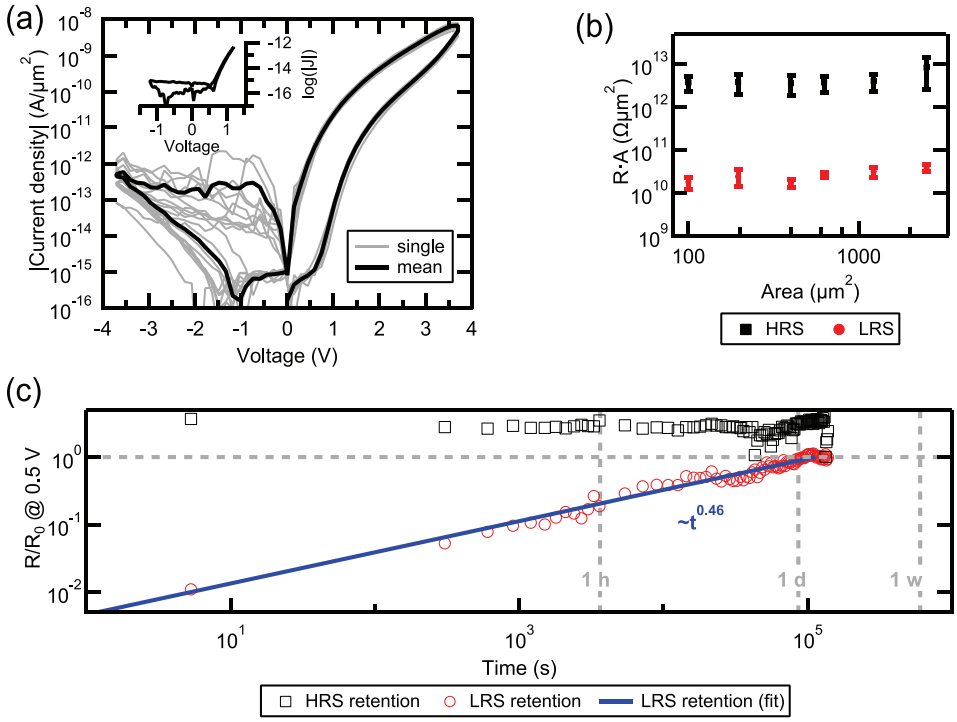

Figure 2. a) $|J|$–V characteristics showing memristive switching of ten individual devices (gray) and their mean value (black). The inset shows a mean $|J|$–V curve for lower voltages that do not induce memristive switching. b) Area dependency of the resistances in HRS (black squares) and LRS (red dots) for 1.2 V bias. Mean values and standard deviations of ten devices for each contact area are depicted. c) Retention time of the LRS (red circles) and HRS (black squares). The resistance evolution of a devices read out with 0.5 V is shown. A fit to the LRS data with a $\propto t^{\alpha}$ power law is further given as solid blue line. (a–c) Voltages are always applied to the Au top electrodes, while the Nb bottom electrodes are grounded.

particular, a power law with $\alpha = 0.46$ fits well the LRS retention characteristics. An α between 0.18 and 0.57 is reported for similar devices,[22,30,33,34] while filamentary devices based on HfO_x show a much longer retention time with $\alpha = 0.02$.[22] After measuring the relaxation process of the LRS resistance, the device is switched to an even higher resistance by applying a negative voltage sweep with $V_{min} = -3.7$ V, and the resistance is read out with the same procedure as the LRS resistance. No distinct trend can be observed in the resistance evolution but a drift toward R_0 is expected on a longer time scale, since the resistance evolution of the LRS does not reveal a further drift toward the HRS resistance. The origin of the rather strong fluctuations in the HRS resistance evolution is unknown and needs to be further investigated in the future. It should be emphasized that the HRS resistance is rather close to the initial resistance ($R_{HRS} \approx 3 \times R_0$) while most of the switching window can be attributed to the difference between the initial resistance and the LRS ($R_{LRS} \approx 0.01 \times R_0$). A much longer retention time of typically more than 10 years is needed for memory applications,[76] but shorter retention times are expected to be beneficial for certain neuromorphic applications.[11] In particular, processing real-world data with spiking neural networks (SNNs) requires not only non-volatile memory elements but also volatile memristive devices with times-scales in the order of the time-scales of the data.[14] One example is reported by Park et al., who utilize volatile analog memristive devices as short-term memory in leaky-integrate-and-fire (LIF) neurons to process sequential data.[77] However, a long retention time is needed for inference in a pattern recognition task.[78,79] Thus, the retention time of the here reported devices has to be enhanced for this application. Nevertheless, the training of pattern recognition networks can be done with memristive devices with moderate retention times,[78,79] as already shown with interface-type memristive devices.[41]

Table 1 further provides a comparison between the devices presented here and those previously reported in literature with similar metal-oxide-based interface-type devices.[30,32,33,42,77] We consider devices that comprise an area-dependent resistance in both HRS and LRS, and that require no external current compliance during switching. The first column of Table 1 shows the devices' material stacks. The electrical parameters extracted from the current-voltage hysteresis curves are the switching window $\Delta R = R_{LRS}/R_{HRS}$ measured with a typical read-out voltage V_{read}, the highest positive and lowest negative voltage used to record the evaluated hysteresis curves ($V_{sw,\,LRS}$ and $V_{sw,\,HRS}$), the maximum absolute value of the current density flowing during switching $|J_{sw,\,max}|$ (i.e., during switching to LRS for all compared devices, thus $|J_{sw,\,max}| = J_{sw,\,LRS,\,max}$), the ratios ΔJ_{sw} of the maximum absolute value of the current densities flowing during switching to LRS $|J_{sw,\,LRS,\,max}|$ and HRS $|J_{sw,\,HRS,\,max}|$, and the absolute value of the current density flowing during read-out the HRS $|J_{read,\,HRS}|$. Furthermore, the retention characteristics at room temperature are compared in two ways. The next to last column provides ΔR, measured after a certain time has elapsed since switching. The last column contains the coefficient α of the $\propto t^{\alpha}$ power law used for fitting the relaxation kinetics (if available).

Table 1. Comparison between different interface-type memristive devices.

Material stack	ΔR at V_{read}	V_{sw} [V]	$\lvert J_{sw,\,max}\rvert$ [A µm^{-2}]	ΔJ_{sw}	$\lvert J_{read,\,HRS}\rvert$ [A µm^2]	Retention	α[a)]
$Nb/NbO_x/Al_2O_3/HfO_2/Au$	100	±3.7	7×10^{-9}	12 000	4×10^{-13}	$\Delta R \approx 1$ after 10^5 s	0.46
(This work)	at 1.2 V						
$Nb/NbO_x/Al_2O_3/NbO_y/Au$	500	+3/−2	2×10^{-7}	142 000	4×10^{-15}	$\Delta R \approx 40$ after 1.5 h	0.18
(ref. [33, 80])	at 0.5 V					($\Delta R \approx 12$ after 10^6 s)[b)]	
$Al/Nb:SrTiO_3/Pt$	25 000	+2/−6	5×10^{-10}	6	2×10^{-15}	–	0.36
(ref. [30])	at 0.1 V						
$Pt/BiFeO_3/Au$	6400	±8	2×10^{-9}	340	2×10^{-14}	$\Delta R \approx 600$ after 24 h	–
(ref. [32])	at 2.0 V					($\Delta R \approx 600$ after 10 y)[b)]	
$Ti/HfO_2/Al_2O_3/Pt$	80	±2	6×10^{-7}	51 000	1×10^{-11}	ΔR constant for 600 s	–
(ref. [42])	at 0.7 V						
$TiN/TiO_x/TiO_2/Pt$	800	+4/−3	7×10^{-5}	84 000	3×10^{-10}	$\Delta R \approx 1$ after <1 s	–
(ref. [77])	at 1.0 V						

[a)]coefficient of the $\propto t^{\alpha}$ power law; [b)]projected values.

2.2. Transmission Electron Microscopy and Electron Energy Loss Spectroscopy

Figure 3a shows a spectral image of a device cross-section recorded with a scanning transmission electron microscope (STEM). Total NbO_x and HfO_2 thicknesses of $d_{NbO_x} = 5\,\text{nm} \pm 2$ nm and $d_{HfO_2} = 4.5\,\text{nm} \pm 0.4$ nm are determined, respectively. The NbO_x/Al_2O_3 interface is rough relative to the film size, leading to local Al_2O_3 thickness variations between ≈2 and 7 nm. Such roughness is also observed in Nb/Al-based tunnel junctions.[85,86] All other interfaces are smooth due to the planning effect of Al on Nb.[85,86] In a high-resolution (HR) STEM image (see Figure S1, Supporting Information), the HfO_2 appears to be polycrystalline, while Al_2O_3 and NbO_x are amorphous. It should be noted that HRTEM measurements of similar functional devices show amorphous HfO_2 (data not shown). Thus, it is expected that the crystalline state is not crucial for memristive switching.

EELS data of the entire layer sequence are shown in Figure 3b, Supporting Information. Here, a line scan of the O–K edge with a vertical step size of 1.75 nm is depicted. The whole HfO_2 and Al_2O_3 appear fully oxidized, and the Nb bottom electrode is also oxidized at the interface to Al_2O_3, as previously reported for similar devices.[80] The spectra of the O–K edges indicate stoichiometric HfO_2 and Al_2O_3, as shown when compared to reference spectra.[81,82] Moreover, an excess of oxygen may be indicated in the center of the Al_2O_3 layer by the pre-peak of the Al_2O_3-related O–K spectra in Figure 3b, Supporting Information. The O_2 seems to be molecular[82,87] or incorporated as peroxide groups,[88] that is, O–O bonds since both can produce the observed pre-peak. We, therefore, interpret this pre-peak as an excess of oxygen. It should be noted that the pre-peak is not stable within the electron beam, as shown in Figure S2, Supporting Information. Moreover, at the same position in the alumina layer, incorporated Ar is found by EELS (see Figure S3, Supporting Information) and energy-dispersive X-ray spectroscopy (data not shown). Since devices without an Al_2O_3 layer show similar memristive switching, as shown in Section 3.1, the elements incorporated into alumina are expected to be not crucial for memristive switching. However, these defects could potentially decrease the overall electrical resistance of the Al_2O_3 layer. The electron energy-loss near-edge structure (ELNES) of NbO_x close to the Al_2O_3 interface can be attributed to a mixture of Nb_2O_5 and NbO_2 since fingerprints of both reference spectra can be found.[67] Moreover, the intensity of the O–K edge decreases with an increasing distance to Al_2O_3, suggesting a continuously decreasing oxygen content in the NbO_x. Note that the ELNES of the NbO_x after the O–K pre-peak has vanished (due to electron irradiation) and now resembles more Nb_2O_5, which could suggest an in situ oxidation of the Nb electrode induced by the electron beam. The low-loss region of the hafnia layer is further analyzed. The corresponding spectra are shown in Figure 3c, together with reference spectra.[83] Despite the broad peak at 34 eV, due to a collective excitation,[89] the HfO_2 spectra show distinct peaks characteristic for the monoclinic structure. The intense plasmon peak at 23 eV, which is sensitive to the oxygen concentration,[83,90] indicates stoichiometric rather than substoichiometric hafnia. Figure S3, Supporting Information shows the evolution of the low-loss regime within the HfO_2 layer. The intensity differences of the plasmon peaks might be due to an oxygen gradient[91] or result from the overlapping low-loss regime of Au and Al_2O_3. These cases cannot be distinguished due to the very small dimensions and the roughness of the films. Figure 3d depicts the Al L_{23} edge measured from the Al_2O_3, which matches well the ELNES of stoichiometric Al_2O_3.[84] For comparison, the L_{23} edge of metallic aluminum is shown, depicting an onset at 4 eV lower energies and a different ELNES than Al_2O_3.

2.3. X-Ray Photoelectron Spectroscopy

XPS and HAXPES measurements were performed at the synchrotron radiation facility PETRA III of DESY (Hamburg,

ADVANCED ELECTRONIC MATERIALS
Open Access
www.advelectronicmat.de

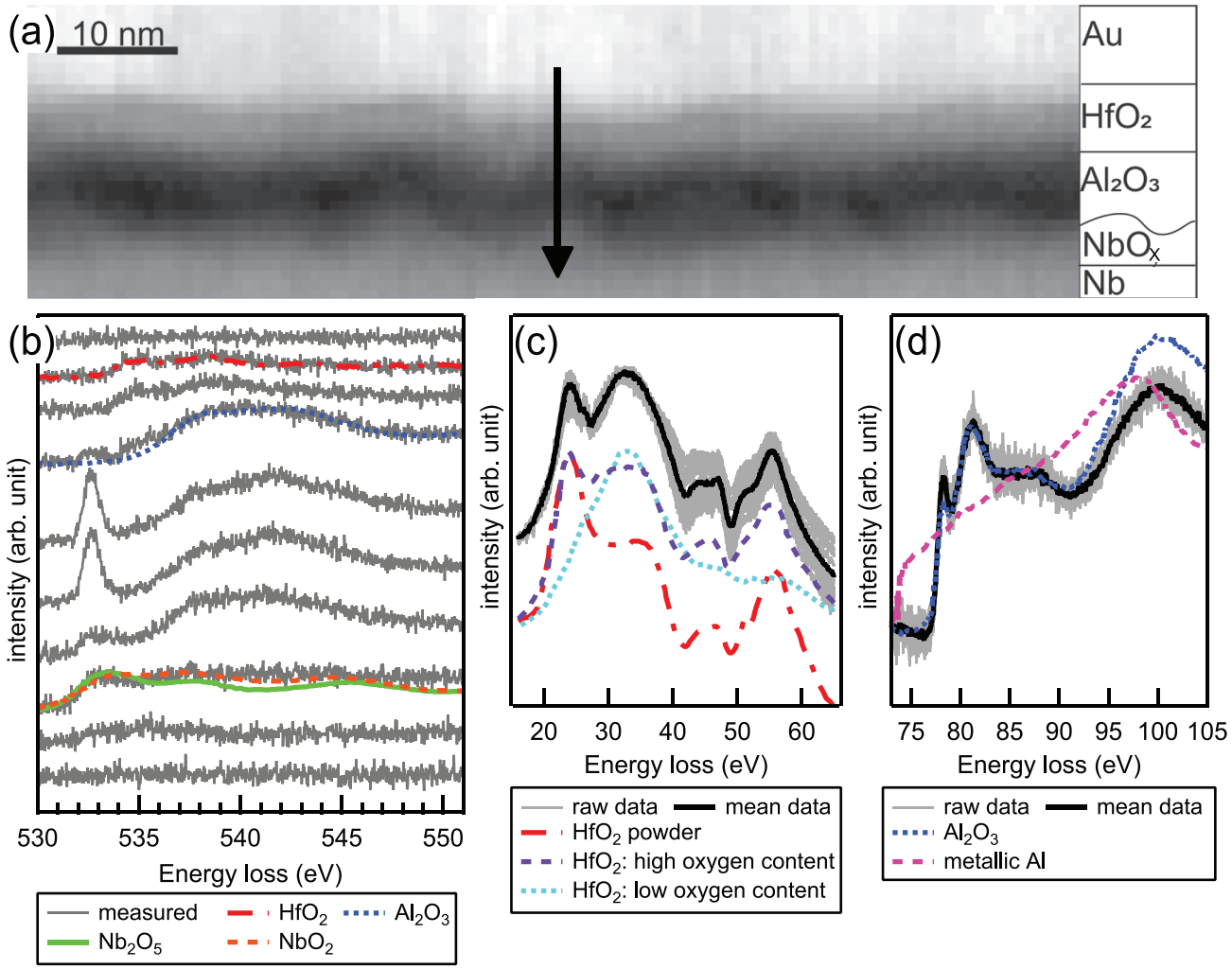

Figure 3. a) STEM recording of a focused ion beam cross section extracted from a functional device in HRS. The black arrow shows where the line scan in (b) was constructed from. In particular, all EELS data related to the pixels of two horizontal lines in (a) are combined as one spectral line in (b). b) EELS line scan of the O-K edge across the whole device stack extracted with a stepsize of 1.75 nm (gray solid lines) together with reference spectra for HfO_2,[81] amorphous Al_2O_3,[82] Nb_2O_5,[67] and NbO_2.[67] c) EELS low loss region of HfO_2 (black solid line: mean value of 36 measurements on adjacent positions, which are shown as gray solid lines) together with reference spectra.[83] d) EELS Al L_{23} of Al_2O_3 (black solid line: mean value of 36 measurements on adjacent positions, which are shown as gray solid lines) together with reference spectra for alumina and metallic aluminum.[84]

Germany) by employing the experimental photoemission endstation ASPHERE III (beamline P04[92]) and the HAXPES endstation at beamline P22,[93] respectively. Details on energy referencing, peak fitting, and in situ electrical characterization can be found in Experimental Section, together with the sample design enabling PES on functional memristive devices (see also Figure S4, Supporting Information). The fabrication of the devices is also described in detail in Experimental Section.

2.3.1. Soft X-Ray Photoelectron Spectroscopy

A memristive device with a 6 nm thin Au top electrode is switched in situ from a high resistance state (HRS1) to a low resistance state (LRS) and back to a high resistance state (HRS2). Au 4*f* and Hf 4*f* core-level spectra for all resistance states are measured. A typical Au 4*f* spectrum is shown in Figure S5, Supporting Information together with a $|J|$–V curve measured in situ, which indicates memristive switching. The Hf 4*f* spectra mainly stem from the Au/HfO_2 interface due to an inelastic mean free path λ of the Hf 4*f* electrons in Au of 1.8 nm estimated using the TPP-2M formula with the parameters provided in ref. [94]. Since ≈95% of the signal intensity originates within 3λ,[95] only the HfO_2 near the Au interface can be probed. The Hf 4*f* spectra are shown in **Figure 4**. Here, a linear function models most accurately the background (gray solid lines). Full width at half maximum (FWHM) values of the doublet features of 1.20, 1.19, and 1.18 eV for HRS1, LRS, and HRS2, respectively, are obtained by fitting, while the Gaussian contribution dominates the Pseudo-Voigt function. Hf $4f_{7/2}$ binding energies (BEs) of 16.44 ± 0.01, 16.56 ± 0.01, and 16.45 ± 0.01 eV are measured for HRS1, LRS, and HRS2, respectively. The errors denote the standard deviation of the BE determined by the peak fitting algorithm. Thus, switching the devices from HRS to LRS and

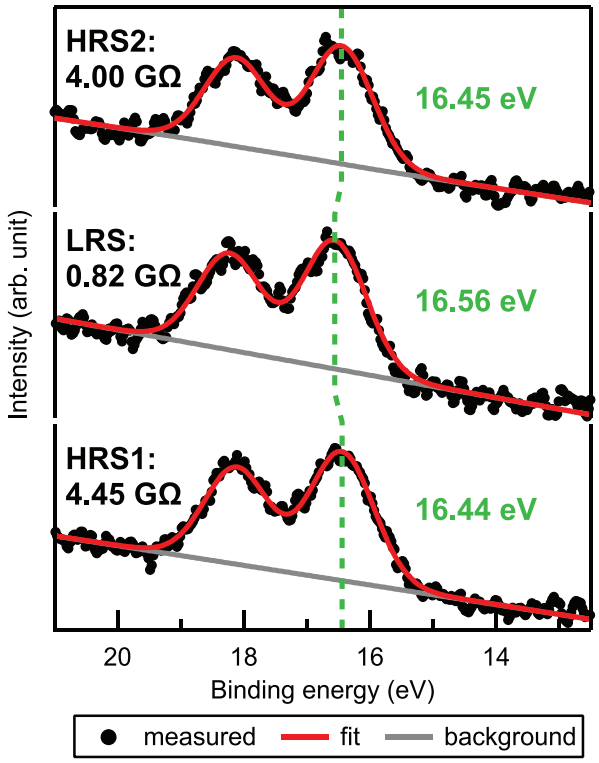

Figure 4. Measured Hf 4*f* spectra (black dots) in HRS1, LRS1, and HRS2, together with fitted peaks (red solid lines) and linear backgrounds (gray solid lines). The dashed green line indicates the shift of the Hf $4f_{7/2}$ position in the different memristive states. Resistances measured with 0.8 V and determined BEs for Hf $4f_{7/2}$ are also given in black and green, respectively.

back again leads to BE shifts of 110 ± 10 meV, with a higher BE for LRS. The difference between HRS1 and HRS2 being within the error margins shows that the core-level switches back to its initial BE. All peaks can be attributed to Hf^{4+} species in HfO_2 with reported BEs between 16.3 and 18.5 eV[48,51–55,96–100] dependent on, for example, the band alignment with adjacent layers or the amount of charges within HfO_2 or adjacent layers. No additional spectral features attributed to sub-stoichiometric HfO_x can be seen, which appear at lower BEs corresponding to metallic Hf with a shift of 2.6–3.8 eV,[51–53,96,97] and to hafnium sub-oxide with smaller shifts.[52–54,96,97,101] As such a signal is linked to filamentary-switching[51–54] with an oxygen vacancy concentration of typically 10^{21} cm^{-3},[102] this shows that the oxygen vacancy concentration in our devices is lower than in filamentary-based devices. This is in agreement with the EELS data indicating stoichiometric HfO_2. Also, additional spectral shape changes commonly observed in the case of chemical changes[55,101] are absent from our spectra. Note that quantitative analyses of the material composition using XPS can lead to an error of less than 5% under best experimental conditions, while relative changes in the composition of less than 1% can be detected,[103] which defines the resolution of XPS. Moreover, while BEs shift of the order of +100 meV, similar to these observed here between HRS and LRS, can be attributed to an additional amount of oxygen vacancies,[101] the hypothesis of such a chemical change can be excluded for the devices studied here (even though the signal-to-noise ratio of the presented Hf 4*f* peaks is low) as the positive bias applied to the Au top electrode cannot lead to an accumulation of (positively charged) oxygen vacancies near the Au interface. Hence, the BE shift toward higher energies in LRS can be attributed to an increased electrostatic potential near the Au interface, the origin of which is discussed in Section 3.2.

Finally, no defects caused by the X-ray radiation during XPS measurement are observed since no radiation-time dependent spectral shifts or additional spectral features, similar to those reported for in operando measurements on ferroelectric $Pb(Mg_{1/3}Nb_{2/3})_{0.72}Ti_{0.28}O_3$ (PMN-PT),[104] are detected here.

2.3.2. Depth-Dependent Hard X-Ray Photoelectron Spectroscopy

Non-destructive depth profiling was done via HAXPES on a memristive device with a 13 nm thin Au top electrode. The measured angle of emission ϑ was varied (see Figure 1), leading to the highest information depth for small angles. All HAXPES spectra of Au 4*f*, Hf $3d_{5/2}$, and Al 1*s* were recorded for three different ϑ and two different resistance states (HRS and LRS) switched in situ. The depth-dependent measurements are called "surface sensitive" ($\vartheta = 15°$), "sub-surface sensitive" ($\vartheta = 41.4°$), and "bulk sensitive" ($\vartheta = 60°$) throughout this work. Since the Au top electrode is relatively thick (13 nm), the signal-to-noise ratio of Hf $3d_{5/2}$ and Al 1*s* decreases significantly with increasing surface sensitivity (i.e., increasing detection angles). The HAXPES recording of spectra with a good signal-to-noise ratio required approximately between 1 and 3 h. Since the LRS significantly relaxes toward the HRS within several hours (see. Figure 2c), the measurement time had to be constant (≈1 h) to ensure that all measurements reflect the same memristive state. Hence, spectra for 41.4° (sub-surface sensitive) and 60° (surface sensitive) were measured two and three times, respectively, and were merged afterward to enhance the signal-to-noise ratio, while the memristive state was refreshed in between (see Experimental Section and Figure S6a, Supporting Information). No Al spectra were evaluated for 60°, and no NbO_x spectra were measured for any ϑ due to the limited information depth of HAXPES. Furthermore, no radiation-induced defects were observed in the HAXPES spectra.

A typical Au 4*f* spectrum is shown in Figure S6b, Supporting Information. Figures S7 and S8, Supporting Information show the raw spectra and the determined backgrounds for Hf $3d_{5/2}$ in HRS and LRS, respectively. The raw Al 1*s* spectra for HRS and LRS are shown in Figures S9 and S10, Supporting Information, respectively. The merged Hf $3d_{5/2}$ and Al 1*s* spectra, together with the peak fits, can be found in **Figures 5**a and 5b for Hf $3d_{5/2}$ and Al 1*s*, respectively, for both HRS and LRS. All spectra show single peaks. The BE and FWHM of the resulting fits are shown in Figure 5c for merged Hf $3d_{5/2}$ and Al 1*s*, respectively, in both HRS and LRS. Error bars denote standard deviations, which are determined by the fitting algorithm. All fitting parameters can be found in Table S11, Supporting Information.

The Hf $3d_{5/2}$ core-level is first investigated in HRS as a function of the angle of emission, revealing BEs between 1662.08 and 1662.28 eV, which can be attributed to Hf^{4+}.[51,100,105] Again, no indication of metallic Hf, and therefore no indication for

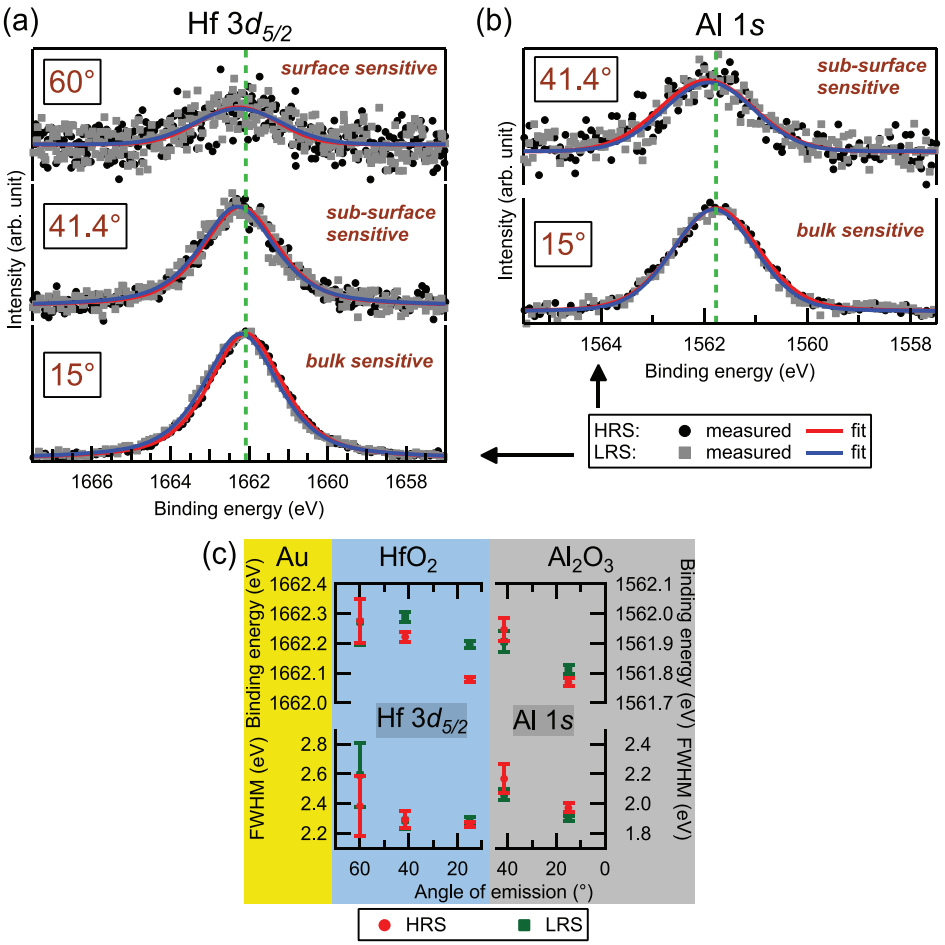

Figure 5. Merged and background-subtracted a) Hf $3d_{5/2}$ and b) Al 1s spectra in HRS (black dots) and LRS (gray squares). Fits of HRS (red solid lines) and LRS (blue solid lines) spectra are also shown. Green vertical dashed lines indicate the peak position in HRS for the bulk sensitive measurements at $\vartheta = 15°$. c) BE and FWHM of Hf $3d_{5/2}$ and Al 1s as a function of the memristive state and depth (emission angle). Error bars denote the standard deviations, which are determined by the fitting algorithm.

a significant amount of vacancies is detectable. In contrast, filamentary-type $Hf_xAl_{1-x}O_y$ memristive devices show a peak feature at 1660.6 eV.[51] Furthermore, the BE increases at larger angles of emission, that is, closer to the Au interface. At the same time, the FWHM does not vary significantly between the sub-surface sensitive and the bulk sensitive measurement. The spectral shape also does not vary, and a chemical difference being responsible for the BE gradient can be excluded.[55,101] Hence, a variation in the electrostatic potential is deduced to be accountable for the BE variation.[48,49] Since the bulk sensitive spectrum is very noisy, the higher FWHM should not be attributed to a chemical change (see Table S11, Supporting Information).

For Al 1s in HRS, BEs of 1561.77 and 1561.95 eV are extracted for the bulk sensitive and the sub-surface sensitive measurement, respectively, indicative of Al_2O_3 since BEs for alumina (Al^{3+}) are reported between 1562.6 and 1563 eV.[106,107] No features of metallic Al are present, which are reported between 1559.6 and 1559.8 eV.[107,108] A similar BE gradient as detected in HfO_2 is visible, suggesting a decreasing electrostatic potential with increasing distance to hafnia. It should again be noted that the noise significantly impacts the peak form of the sub-surface sensitive Al 1s spectrum at 41.4° (see Table S11, Supporting Information).

Next, Hf $3d_{5/2}$ peaks are evaluated in the LRS. Again, no metallic Hf feature is present (see Figure 5a). BEs shift to higher energies by ≈120 and 70 meV for bulk sensitive and sub-surface sensitive measurements, respectively, as shown in Figure 5c. No significant BE shift can be measured for the surface sensitive spectrum. However, the standard deviations for both HRS and LRS are larger than 70 meV for the surface sensitive measurements so that any BE shift below this value cannot be reliably resolved. Nevertheless, an obvious trend is visible toward higher BE in LRS, with the most pronounced shift near Al_2O_3. The FWHM for bulk sensitive and sub-surface sensitive measurements do not change, and no additional peak features appear (Figure S12a, Supporting Information). Thus, no electrical bias-induced chemical change can be detected.[55,101] The shifted BE is hence attributed to a change in the electrostatic potential within hafnia toward a higher potential in LRS. No additional peak features are present for Al 1s as well (see Figures 5b and S12b, Supporting Information). Here,

ADVANCED ELECTRONIC MATERIALS
Open Access
www.advelectronicmat.de

for 15° (bulk sensitive) and 41.4° (sub-surface sensitive), the BEs shift in opposite directions (see Figure 5c). Near HfO_2, the BE shifts by −40 meV (41.4°), and deeper in Al_2O_3, the BE shifts by +40 meV (15°). However, the BE difference between HRS and LRS for 41.4° (near HfO_2) is within one standard deviation of the uncertainty of the fit. The peak width is getting smaller in LRS (≈0.1 eV) for the bulk sensitive spectrum. The peak shape of the sub-surface sensitive measurement is not evaluated as explained above. Altogether, the BE variation in alumina can be ascribed to a variation in the electrostatic potential. In particular, the potential decreases at the HfO_2 interface and increases further inside in LRS.

3. Discussion

3.1. Current Transport Mechanism

The $|J|$–V curves (Figure 2a) show a high non-linearity and a rectification of several orders of magnitude. This can be attributed to a Schottky-like contact which can form due to a direct metal/semiconductor contact but can also be established with a thin oxide layer between metal and semiconductor.[69,70] In particular, a Pt/HfO_2(5 nm)/n-GaAs Schottky diode has already been reported.[109] According to literature, current transport in the devices under study can thus be attributed to thermionic emission[69,70,109] for low applied voltages (but above a memristive state-dependent threshold) in combination with an intrinsic current compliance dominant for high voltages (see Section S13, Supporting Information for a more detailed explanation), as also reported for similar devices.[33] A positively charged space charge region (SCR) within an n-type semiconductor is consistent with the positive forward bias on the high work function Au top electrode. Thus, the electrostatic potential in the semiconductor increases with the distance to Au. In contrast, the potential within HfO_2 and Al_2O_3 decreases with distance to the gold electrode for both memristive states, as revealed by HAXPES non-destructive depth profiling. Therefore, the NbO_x at the interface to Al_2O_3 is most probably responsible for the rectifying properties leading to a two-terminal MIS structure with a bilayer HfO_2/Al_2O_3 insulator. While stoichiometric Nb_2O_5 is known to be a good insulator,[67] it is reported that even a small reduction leads to an n-type semiconducting behavior.[67,68] Since EELS data indicate a mixture of Nb_2O_5 and NbO_2 with an oxygen gradient, semiconducting NbO_x can be expected.

Further information on the effect of the single material layers on the device functionality can be obtained by exchanging or omitting some of the layers and comparing the $|J|$–V characteristics with those of the reference devices. To this end, three additional device compositions were investigated (see Experimental Section for fabrication details). The corresponding $|J|$–V curves measured on devices with a top electrode size of 625 µm² are shown in **Figure 6**, where the insets show the respective material stack. Figure 6a displays the same data as shown in Figure 2a for a better comparison to the characteristics of the other devices. The $|J|$–V switching characteristics of ten individual devices and the corresponding mean curve is shown, together with the mean read-out characteristics. Figure 6b depicts the $|J|$–V characteristics of ten devices having a Hf bottom electrode instead of Nb. The Hf should be oxidized at the interface to Al_2O_3, similar to the Nb electrode. A significantly different performance is revealed compared to the reference devices in Figure 6a. For instance, a significant current can only be measured for positive voltages higher than 4.5 V when applying voltage sweeps with ±5 V amplitude. Moreover,

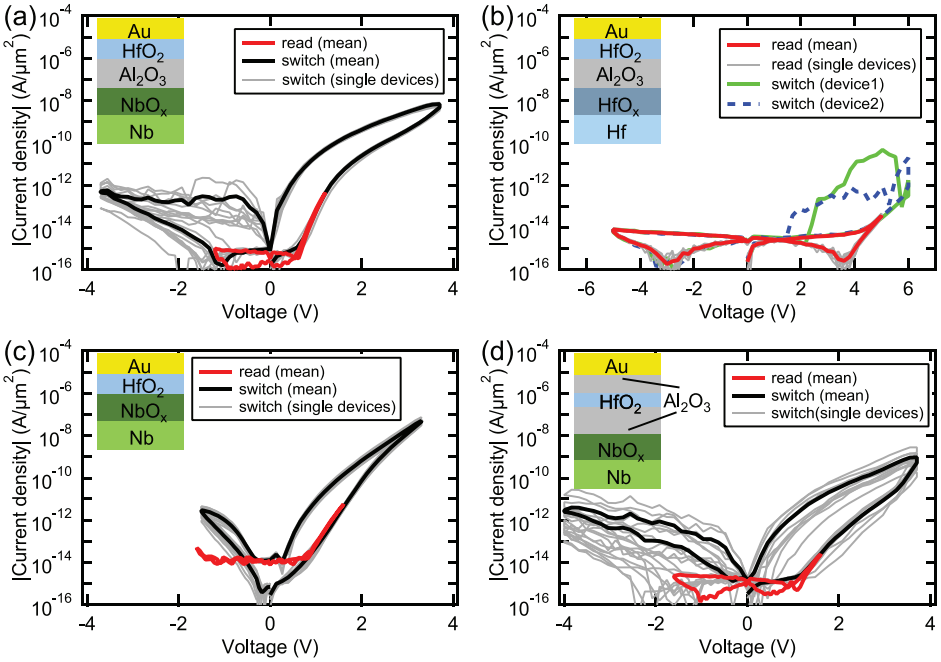

Figure 6. a) $|J|$–V characteristic of reference devices and b–d) devices with different material stacks. The respective material stacks are shown as insets. Each black and red solid line shows the mean $|J|$–V data of ten individual devices.

no analog memristive switching is observed even at higher voltages. However, a few devices show a threshold switching behavior[110] when the positive bias is increased up to 6 V (see green solid line and blue dashed line). Note that this behavior differs strongly for different adjacent devices and is not well reproducible. Thus, replacing the Nb bottom electrode with Hf drastically changes the devices' $|J|$–V characteristics and the memristive switching process. This demonstrates the relevance of the bottom electrode on the device characteristics. Figure 6c shows $|J|$–V characteristics of ten devices without any Al_2O_3. Here, the qualitative behavior is the same as for the reference devices, that is, diode-like current transport and analog memristive switching for voltages above a certain threshold. However, the devices do not allow to apply voltages with an absolute value as high as the other device types, especially for negative bias. Therefore, V_{max} = 3.3 V and V_{min} = –1.5 V are used to induce memristive switching. This clearly shows that memristive switching in the reported devices does not rely on the Al_2O_3 layer. However, the Al_2O_3 leads to less degradation of device performance over time (not shown) and significantly increases the retention time in similar devices.[33] The $|J|$–V curves of ten device with an additional 2.5 nm thin Al_2O_3 layer between HfO_2 and Au can be found in Figure 6d. The lower Al_2O_3 and the HfO_2 layer are thinner so that the overall oxide thickness increases by ≈1 nm. The Nb bottom electrode is most probably oxidized again. These devices show qualitatively the same behavior as the other devices with Nb bottom electrodes. Thus, a device with an Au/Al_2O_3 interface leads to similar performance as a device with an Au/HfO_2 interface. The overall resistance, however, is increased compared to the reference devices and the device variability for positive and negative bias is significantly larger. For switching sweeps, voltage amplitudes of V_{max} = 3.7 V and V_{min} = –4 V are used.

We can conclude that current transport is dominated by the SCR within NbO_x while the HfO_2/Al_2O_3 double oxide layer acts as intrinsic current compliance. This is found by the tremendous change in the electrical characteristics when replacing the Nb bottom electrode with a Hf bottom electrode. It further agrees with the missing positively charged SCR in hafnia and alumina, as revealed by the depth-dependent HAXPES measurements, and with the composition of the NbO_x, as determined by EELS.

3.2. Memristive Switching Mechanism

The XPS and HAXPES spectra reflect the memristive switching mechanism in the following way. A net potential increase in HfO_2 is shown by a combination of the Hf $3d_{5/2}$ data (see Figure 5c) and the Hf 4*f* spectra (see Figure 4). In particular, Hf $3d_{5/2}$ spectra reveal a higher potential increase at ϑ = 15° and thus near the Al_2O_3 interface than at the sub-surface sensitive measurements (ϑ = 41.4°). The measured signals are too noisy to distinguish a potential peak shift for surface sensitive measurements (near the Au interface). The Hf 4*f* spectra, which stem from the Au/HfO_2 interface, indicate a potential increase near the Au interface as well. Movement of negatively charged oxygen ions or positively charged oxygen vacancies within hafnia would lead to an increased potential at one interface together with a decreased potential at the opposite interface. Moreover, the exchange of negatively charged oxygen ions between HfO_2 and Al_2O_3 can also be excluded since the positive voltage applied to Au to switch to LRS would attract these ions, and the hafnia would charge negatively. Furthermore, positively charged oxygen vacancies cannot enter HfO_2 from Al_2O_3 when switching to LRS since the electric field under positive bias repels them. Thus, ion movement can be excluded with high probability.

Here, we suggest charging and discharging of localized traps within the HfO_2 layer or at the HfO_2/Al_2O_3 interface as an alternative switching mechanism. Probable candidates for these traps are oxygen vacancies. Simulations using a hybrid density functional suggest that these vacancies are singly positively charged (i.e., one electron is trapped) or neutrally charged (i.e., two electrons are trapped) if the Fermi level is located between 3.7 and 4 eV or 4 and 5.5 eV above the HfO_2 valence band maximum (VBM), respectively.[111] The theoretical barrier height[69,70] between HfO_2 and Au is 3.1 eV with an Au work function of 5.3 eV[112] and a HfO_2 electron affinity of 2.2 eV[99] leading to a Fermi level position of 2.6 eV above the VBM when considering a band gap of 5.7 eV.[99] However, the actual barrier can deviate strongly (toward lower effective barriers) from these theoretical values,[48,69,70] and this can be expected for the multi-layer device structure here. Thus, neutral or singly positively charged vacancies in thermodynamic equilibrium are reasonable since a lower effective barrier leads to an increased Fermi level with respect to the VBM. Applying a positive potential to Au can lead to a positive charging of the vacancies since electrons can be ejected.[28,30,43] This agrees with the BE shifts toward higher energies in LRS. Moreover, additional positive charges within the HfO_2 layer influence the potential drop across the Al_2O_3 layer as well. Here, negative image charges may lead to the decreased potential at the HfO_2/Al_2O_3 in LRS and thus to the decreased potential drop across alumina as indicated by the depth- and state-dependent BEs of the Al 1*s* spectra (see Figure 5c). The decreasing FWHM of Al 1*s* spectra are consistent with a decreasing voltage drop across this layer (see Figure 5c) since the width of photoelectron spectra can increase due to an increased voltage drop across the probed layer.[100,105] No significant changes in the FWHM of Hf $3d_{5/2}$ and Hf 4*f* are found. However, a potential of 0.9 V across HfO_2 is estimated to lead to a Hf $3d_{5/2}$ spectral broadening of 0.1 eV in ref. [100]. Thus, the smaller change in the potential in the HfO_2 layer cannot be detected through a change in FWHM within the standard deviation of the determined peak width.

The potential variation is used to estimate the amount of charges involved in switching, as shown in detail in Section S14, Supporting Information. Two scenarios are considered, that is, uniformly distributed bulk charges and charges located at the HfO_2/Al_2O_3 interface, in agreement with ref. [30]. A bulk charge density of $N_B = 1.6 \times 10^{19}$ cm^{-3}, and an interface charge density of $N_I = 4.7 \times 10^{12}$ cm^{-2} are estimated. It should be noted that the estimated charges are not the maximum amount of charges involved in switching for two reasons. First, recording a single Hf $3d_{5/2}$ spectrum takes about 19 min, during which the respective energy range is scanned six times, and the single sweeps are then combined into a single spectrum. In this time span, a relaxation toward HRS takes place

(see Figure 2c). Thus, the determined BE shift between HRS and LRS reflects the mean potential difference within this time frame. Second, the BE shift at the bulk sensitive measurements (15°) is used to estimate the potential increase at the hafnia/alumina interface. Yet, the real potential increase is higher since the photoelectron spectra for 15° angle of emission include contributions from all parts of the HfO_2 layer. The potential only linearly contributes to the estimated charge densities (see Equations (S14.2) and (S14.4), Supporting Information). Thus, the order of magnitude calculated for both densities does only change if the actual potential increase deviates from the estimated increase by one order of magnitude, which is not to be expected. Since the oxygen vacancy density in physical vapor deposition (PVD) processed HfO_2 is reported to be in the order of 10^{19} cm^{-3},[113] the estimated value of N_B is reasonable. Moreover, this vacancy density is too small to be detected by photoelectron spectroscopy, which allows for finding differences in the material composition down to $\approx 1\%$.[103] This explains why no fingerprints of oxygen vacancies can be found in the spectra. The estimated value of N_I is also reasonable since charge densities of up to 7.8 $\times$ 10^{12} cm^{-2} at a HfO_2/GaN interface are reported.[114] Thus, bulk charges in HfO_2, interface charges at the alumina interface, or a combination of both can explain the potential variation.

In addition, filamentary switching is likely to be suppressed in the reported devices due to the low amount of vacancies compared to other devices showing filamentary switching together with spectral fingerprints of oxygen vacancies.[50,51,54] In this respect, first principles-based simulations reveal that for efficient nucleation and growth of oxygen-deficient filaments in HfO_x an x in the range of 1.50–1.75 is optimal.[115] This is experimentally supported by Park et al.,[22] who show a filamentary-type switching for $x = 1.80$ and an area-type switching process for $x = 1.98$. HfO_2 films, which are stoichiometric after deposition, can also lead to filamentary switching if an initial electro-forming step reduces the HfO_2 locally.[59] This is avoided in our devices by using a noble metal top electrode and an Al_2O_3 film acting as a diffusion barrier for oxygen ions[33,57] as adjacent layers.

In summary, the memristive switching in the devices under study can be directly correlated with the electrostatic potential within HfO_2 and, thus, with the charge state of electron traps which are most probably oxygen vacancies. Indeed, HfO_2 is widely investigated as charge trapping layer in CTF memory.[66] Here, trapped charges are assumed to modulate the conduction channel in MOSFETs. Moreover, memristive devices based on charging and discharging of traps within HfO_2 have already been reported[42,56,63] without spectroscopic evidence. The influence of the potential variation on the device resistance is explained in the next section.

3.3. Device Model

A schematic band diagram of the qualitative device model can be found in **Figure 7**. A band diagram is used to visualize the involved potential profiles and barriers. The widths of the layers are drawn to scale, while the band alignment and the amount of band bending are drawn qualitatively. The current

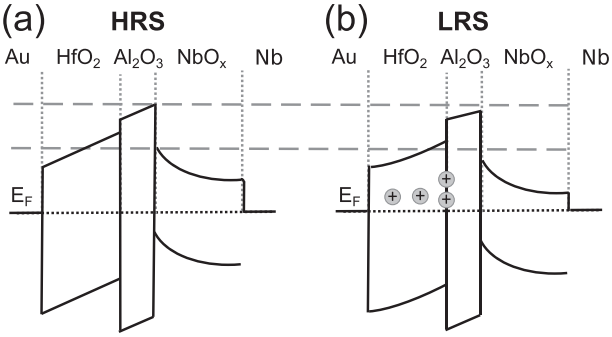

Figure 7. Band diagram of the device model in a) HRS and b) LRS. Only the additional positive charges in LRS arising from electron de-trapping are schematically indicated.

transport is dominated by the SCR within NbO_x while hafnia and alumina act as intrinsic current compliance. The current through the dielectrics can be assumed to be assisted by defects so that a significantly high current can flow even for ≈6.5 nm insulators. In particular, the current through Al_2O_3 can be assumed to be dominated by the thinnest parts (≈2 nm) of the layer (see the width of alumina relative to hafnia in Figure 7). The total charge distribution within the multi-layer stack is unknown. The HfO_2 and Al_2O_3 bands are drawn linearly in HRS in Figure7a for simplicity but can have a more complex shape. The upward band bending in the dielectrics is indicated by the HAXPES data, while the downward band bending in the semiconducting NbO_x is extracted from the forward bias of the diode-like characteristics. A significant amount of negative charges at the Al_2O_3/NbO_x interface is deduced to account for the band profile. Additional positive charges in the hafnia layer and at the HfO_2/Al_2O_3 interface in LRS, as qualitatively indicated in Figure 7b, are attributed to electron de-trapping from neutral or singly positively charged oxygen vacancies. Bulk traps, interface traps, or a combination of both can explain the switching.

The additional positive charges in the HfO_2 layer in LRS influence the charge distribution within the buried NbO_x such that the built-in potential decreases. This is similar to $HfO_2/SiO_2/Si$ gate stacks, in which positive charges within HfO_2 lead to a decreased upward band bending within silicon.[116] Furthermore, positive charges within interfacial oxide layers in metal/semiconductor Schottky contacts are also reported to decrease the upward band bending.[70] Thus, the effective barrier height and, thereby, the overall device resistance decrease due to positive charging of electron traps in HfO_2. Switching the device back to HRS results in the initial charge distribution and, thereby, in the initial resistance. The proposed model can also explain the different current fluctuations for positive and negative bias (see Figure 2a and 6a). The devices are initially in the HRS, and the voltage is swept in positive direction first. For low voltages, the current transport is dominated by thermionic emission, and no memristive switching takes place. An intrinsic current compliance becomes dominant for voltages high enough to induce memristive switching (see Section S13, Supporting Information). The current density shows low fluctuations for both low and high positive voltages. When the voltage is swept back to 0 V, the device resistance relaxes toward HRS,

even without applied bias (see Figure 2c). Thus, switching toward HRS takes place for all negative biases. The electron trapping can be expected to cause the observed noise for negative bias.[117] This effect is probably only visible for switching to HRS because the current density during switching to LRS is orders of magnitude higher. Besides, an additional higher variability for negative bias can potentially be explained by the inhomogeneous Al_2O_3 layer (see Section 2.2) if the current transport for negative bias is restricted by the alumina. Moreover, the proposed model does also explain why the device with Hf bottom electrode does not show interface-type memristive switching (see Figure 6b). In contrast to the NbO_x, no SCR exists in the HfO_x below alumina. Thus, a variation in the charge distribution in HfO_2 does not impact the current transport as significantly as for the reference device since no SCR is modulated.

It is further estimated that the NbO_x cannot completely screen the built-in potential due to its thickness of $d_{NbO_x} \approx 5\,\text{nm}$. For an estimate, the standard formula for the Debye length λ_D is used[69,118] (see Equation (S15.1) and Section S15, Supporting Information). The relative permittivity of NbO_x is assumed to be between 10 (NbO_2) and 41 (Nb_2O_5).[68] Thus, 63% of the built-in potential can be screened in NbO_x (i.e., $\lambda_D = d_{NbO_x}$) if the doping concentration is between 2.9×10^{17} and 1.2×10^{18} cm^{-3}. These are reasonable doping concentrations since concentrations of up to 6×10^{19} cm^{-3} for Nb_2O_{5-x} are reported.[68,119] However, a complete screening can be expected for $\approx 10\lambda_D = d_{NbO_x}$, as is the case for GaAs.[69] This requires a doping concentration between 2.9×10^{19} and 1.2×10^{20} cm^{-3}. Since an increase in charge density in the order of 10^{19} cm^{-3} in HfO_2 (with $d_{HfO_2} \approx d_{NbO_x}$) is estimated to have a significant impact on the charge distribution within NbO_x, such a doping concentration is unlikely in the reported devices, and part of the built-in potential should drop in the Nb bottom electrode. Moreover, in the latter case, ≈95% of the built-in potential would be screened within 1.5 nm, and thus direct tunneling is expected to have a significant impact on current transport so that no diode-like behavior would occur. More details about these calculated results can be found in Section S15, Supporting Information.

In summary, the experimental findings consistently indicate that our devices consist of a two-terminal MIS-like structure in which electron traps within the insulator modulate the space-charge region of the semiconductor and, thereby, the overall device resistance. This is consistent with the results of ImpSpec conducted on the reference devices, performed by Marquardt et al. and reported in the companion paper.[74] Here, the kinetics of the set process and of the retention imply charging of traps rather than ion movement. Furthermore, quantitative model parameters describing current transport in HRS and LRS and switching dynamics are given. In particular, current transport is described by thermionic emission with an effective barrier height of 0.84 and 0.675 eV, as well as an ideality factor of 3.71 and 4.9 in HRS and LRS, respectively. A series resistance of 12 kΩ and a reach-through[120] complete the current transport model. The results from Marquardt et al. are in agreement with the qualitative model proposed here, which could be applied to explain memristive switching phenomena in other devices as well.

Similar device models have already been reported by other groups without spectroscopic evidence. In this respect, Mikheev et al.[30] explained memristive switching in Pt/Nb:$SrTiO_3$ (NSTO) by a modulation of the Schottky barrier height by a variation in trapped charges within an inter-layer consisting of carbon contamination between metal and semiconductor and a potentially damaged single crystalline NSTO interface. Kim et al. investigated TiN/NbO_z/TiO_2/NbO_z/Pt memristive devices.[43] Here, electrons are reported to be ejected from traps ascribed to Ti-sites in the upper NbO_z layer (adjacent to Pt) by applying a positive voltage to the Pt electrode. This modulates the Schottky barrier of the NbO_z/Pt interface. The NbO_z is a mixture of ≈60% Nb_2O_5 and 40% NbO_2. Gao et al. report on an optoelectronic indium tin oxide (ITO)/NSTO junction in which memristive switching is induced by Schottky barrier modulation due to electron de-trapping while illuminated with light.[36] Furthermore, charge trapping at an HfO_2/Ti interface is reported as a memristive switching mechanism.[42] In addition, devices are reported in which resistance switching is based on electron trapping in HfO_2 which changes the bulk conductivity of hafnia and, thereby, the overall resistance, while a rectifying barrier is unaffected.[56,63] Moreover, an MIS model that explains memristive switching in Au/NSTO and Au/$BaTiO_3$/NSTO devices through electron trapping and de-trapping in an interfacial layer is given by Fan et al.[34] Their model is supported by scanning Kelvin probe microscopy (SKPM) and piezoresponse force microscopy (PFM) studies on both the NSTO substrate and the $BaTiO_3$ layer, respectively. Thus, we show spectroscopic evidence on functional devices for Schottky barrier modulation by electron trapping/de-trapping in general and for electron trapping/de-trapping in HfO_2 in particular, in agreement with the other models.

The device model allows to propose methods for engineering the device characteristics for specific applications. In this respect, the defect density in the HfO_2 could be tuned by adjusting the sputter deposition parameters which affects the switching window.[22,121] A strong impact of the top electrode's work function and metal–insulator interface quality on the read-out and switching parameters is further expected, since these properties crucially affect the current transport in interface-type devices. Reducing the roughness between the NbO_x and the Al_2O_3 might lead to less device variability. Finally, the device model can be exploited to deduce design rules for the integration of the devices into CMOS technology. First, the amount of charge traps involved in switching should be larger than the amount of charges in the SCR so that the traps can have a significant impact on the depletion region. Second, the insulator should guarantee an intrinsic current compliance to protect the device from dielectric breakdown while simultaneously allowing a significant current flow. Third, the density of oxygen vacancies in the insulator must be low enough to prevent filament formation. Fourth, for a back-end-of-line (BEOL) compatible process and, thereby, for a potential 3D integration and a more flexible chip design, CMOS-compatible semiconductors such as amorphous or poly-crystalline Si could be explored. Fifth, a fab-friendly metal that forms a rectifying barrier with the semiconductor should be used. Sixth, the overall current density should be orders of magnitude higher than in the reported devices to enable a geometrical scaling to the nanometer regime while obtaining a measurable read-out current (see inset of Figure 2a).

4. Conclusion

In summary, a comprehensive characterization of analog memristive switching devices composed of $Nb/NbO_x/Al_2O_3/HfO_2/Au$ showing diode-like $|J|$–V characteristics is reported. The stoichiometry of HfO_2 and Al_2O_3 is confirmed by EELS and HAXPES, while an excess of oxygen and argon in the center of the Al_2O_3 is indicated by EELS. The oxidation state of the NbO_x is determined by EELS to be a mixture of Nb_2O_5 and NbO_2 with decreasing oxygen content toward the Nb bottom electrode. Non-destructive depth-dependent HAXPES and XPS measurements show that the space-charge region that accounts for the diode-like behavior is neither located in the HfO_2 nor in the Al_2O_3 layer. Memristive state-dependent core-level shifts indicate that the charging of vacancies within HfO_2 is responsible for switching. The experimental results suggest a purely electronic origin of memristive switching in the investigated devices. We could not find any hints of ionic drift as a source for the observed switching behavior. Devices with adjusted layer stacks reveal that the diode-like behavior is caused by the NbO_x layer, while Al_2O_3 is not crucial for the memristive switching. The proposed memristive device model consists of a two-terminal MIS-like structure in which electron traps within the insulator modulate the space-charge region within the semiconductor and, thereby, the overall device resistance. While similar memristive device models have been reported before, we present here spectroscopic evidence on functional devices for the charging and discharging of electron traps as the origin of memristive switching in such devices.

The worked-out model is in agreement with the companion paper Marquardt et al. that exploits ImpSpec to probe the current transport and switching kinetics of the same devices.[74] Based on two different experimental approaches (XPS/HAXPES and ImpSpec), our findings strongly indicate an electronic charging and discharging of traps as the fundamental origin of resistive switching in our devices, instead of ionic drift.

5. Experimental Section

Device Fabrication: In the standard process, all layers were deposited using DC magnetron sputtering without breaking the vacuum with a base pressure of less than 5×10^{-7} mbar. The devices were fabricated on 100 mm Si wafers passivated by 400 nm thermally oxidized SiO_2. Metallic Nb and Al were first deposited in Ar atmosphere. The following deposition of HfO_2 in a reactive Ar/O_2 gas mixture using a metallic Hf target leads to the oxidation of the Al layer and, to some degree, of the Nb layer.[80,121] The Au top electrode was deposited in an Ar atmosphere. The device patterning was performed by standard optical lithography, lift-off processes, and Au etching in potassium iodide to get different electrode areas. The fabrication process was developed by Hansen et al. for similar devices (with NbO_y instead of HfO_2)[33] and is described in more detail in refs. [33, 121]. The HfO_2 layers investigated here were produced in exactly the same process as the NbO_x in refs. [33, 80, 121], that is, with a total process pressure of 1.21×10^{-2} mbar in poisoned mode (7 sccm Ar, 23 sccm O_2), a discharge power of 100 W and with a target to substrate distance of ≈53 mm. The Hf bottom electrode for the device shown in Figure 6b was deposited with the same sputter parameters as the Nb bottom electrode. The upper 2.5 nm thin Al_2O_3 layer for the device in Figure 6c was deposited with the same process pressure, gas composition, and power as the HfO_2. Here, the HfO_2 and Al layers were deposited slightly thinner than for the reference device so that the overall $Al_2O_3/HfO_2/Al_2O_3$ tri-layer is ≈1 nm thicker than the insulator bi-layer of the reference devices.

Different device structures were built for this work:

(i) Reference devices with structures described in ref. [33] were fabricated. Here, six different contact areas ranging from 100 to 2500 μm^2 are arranged across the wafer. Furthermore, a 720 nm thick Ti wiring layer covers the top electrodes and connects them to Ti contact pads. A SiO_x layer is needed as insulation between the wiring layer and the mesa structures. The devices shown in Figure 6 were also fabricated with the same design.

(ii) Functional devices for the XPS and HAXPES measurements were fabricated with a different design. Here, the top electrode has to be much thinner and must not be covered with a wiring layer because the information depth of HAXPES is in the order of a few ten nm, while it is even less for lower energetic X-rays also used in this work.[47,51] The device structure is shown in Figure S4, Supporting Information which is inspired by ref. [105]. The Au top electrodes are electrically connected to Ti contact pads by Ti wiring lines, which only cover a small percentage of the device area. The total top electrode areas of the investigated devices are 13650 μm^2. 9000 μm^2 are not covered by insulation or wiring layers allowing to probe the devices with PES. To obtain functional devices, the top electrode has to form a continuous film. Since thin gold films are known to grow in an island-like structure on ceramics,[122] an optimization of the top electrode deposition process has been performed. In the sputter deposition process, the thinnest continuous film produced has a thickness of 13 nm. A device produced that way was probed by HAXPES. The Au was thermally evaporated to get even thinner continuous films of 6 nm. Therefore, the respective wafer had to be transferred from the sputter deposition chamber to the evaporation chamber being exposed to normal atmosphere for less than 5 min. The wafers with structures (ii) not only contain devices with the described structures but also test structures as described in (i). These devices only work if the Ti wiring layer has no direct contact with HfO_2. Thus, measuring the electrical characteristics of these test structures verified that the deposited Au formed continuous layers.

Electrical Measurements and Memristive Switching: The bias voltage was applied to the Au top electrode while the bottom electrode was grounded. Trapezoid-shaped voltage sweeps were applied, where the voltage was increased from 0 V to the positive maximum bias V_{max}, then decreased to the negative bias V_{min} and increased again to 0 V. In total, 100 voltage steps with a total bias time of 220 s were used. The read-out characteristics of the devices with $Nb/NbO_x/HfO_2/Au$ material stack were recorded with a total bias time of 16 s, which leads to the higher noise level in Figure 6(c) (red line). In situ switching to HRS or LRS in XPS/HAXPES experimental chambers was done with trapezoidal-shaped voltage sweeps of one polarity only (50 steps, 110 s). All data from the reference wafer (Figure 2) and the devices with alternative layer stacks (Figure 6) were measured with an HP4156A semiconductor parameter analyzer. Electrical characterization and memristive switching at the synchrotron beamlines were done with an Agilent E5260 source measurement unit (SMU) at beamline P04, and an Agilent B2912A SMU at beamline P22, respectively. The X-ray beam was never directed to the sample while applying bias to the devices.

The spectra for emission angles of 41.4° (sub-surface sensitive) and 60° (surface sensitive) were measured two and three times for each memristive state, respectively, and the state was refreshed in between. First, the spectra were recorded for HRS for all three angles. Afterward, the device was switched to an LRS with a unipolar voltage sweep with $V_{max} = 4$ V. To guarantee that all spectra for all detection angles were recorded for the same resistance state, a current compliance of 30 μA was utilized. Refreshing the resistance state to one and the same level was possible, and the device's retention was long enough to record data

for two distinct resistance states, as shown in Section S6, Supporting Information. The higher read-out voltage of 1.8 V was necessary because the noise level of the *I*–*V* measurement within the vacuum chamber did not allow to use lower voltages. However, the device state was not significantly affected by the higher read-out voltage (see Section S6, Supporting Information).

TEM and EELS: TEM characterization was performed using an FEI Titan^3 at an acceleration voltage of 300 kV with spherical aberration (C_s) probe correction and monochromator. The EEL spectra were acquired with a GIF Quantum Dual EELS detector. To probe the whole material stack, a focused ion beam lamella was extracted from a functional device in HRS of structure (ii) with a 13 nm Au top electrode. The line scan in Figure 3b is constructed from a spectral image by summing all spectra horizontally and binning two of these lines to obtain a vertical step size of 1.75 nm.

XPS and HAXPES: The Au top electrode was electrically connected to a common ground with the analyzer during photoelectron spectroscopy. During HAXPES measurements, also the bottom electrode was connected to the common ground leading to defined electrical boundary conditions when evaluating potential profiles. All recorded Hf and Al spectra were aligned with the Au $4f_{7/2}$ peak of the top electrode at 84.0 eV BE. It should be emphasized that this provides an energy reference relative to the Fermi level of the Au rather than an exact alignment of the energy with $E_F = 0$ eV. All core-level spectra were fitted with the XPST add-on for IGOR Pro software (WaveMetrics), which utilized the Pseudo-Voigt function described in ref. [123]. Here, the Voigt profile was approximated by a Lorentzian–Gaussian sum function. Shirley-type backgrounds[124] were used for spectra with a sufficient signal-to-noise ratio. Otherwise, linear backgrounds were used. The XPS measurements with soft X-rays were measured with an X-ray energy of 1550 eV, a beam spot diameter of <15 µm, and an energy resolution of ≈200 meV. The HAXPES spectra were obtained with an energy of 7000 eV, a beam spot of 20×20 µm^2, and a total experimental energy resolution of ≈300 meV. Depth-dependent information was obtained by measuring HAXPES spectra from different angles of emission. This was achieved by rotating the sample relative to the analyzer and also to the X-ray beam so that the footprint of the beam was elongated in one direction with a factor of $1/\sin(\vartheta)$ (i.e., a maximum footprint of 20×80 µm^2 for the bulk sensitive measurements at 15°). All PES measurements were conducted at 300 K.

Au 4*f* spectra were fitted with a fixed spin-orbit splitting of 3.7 eV, an intensity ratio of 0.75 for f-orbitals and the same FWHM for both components.[125] For XPS measurements with the 6 nm top electrode, two doublet features assigned to surface states and bulk Au[126] were detected (see Section S5, Supporting Information). For HAXPES measurements with a 13 nm Au top electrode, a single asymmetric doublet peak (see Section S6, Supporting Information) with additional features at higher BE was detected as it was usually observed for XPS spectra of gold and other metals.[123] This asymmetry was incorporated into the fit by using an asymmetric Pseudo-Voigt function.[123] No resistance state-dependent peak shift was observed for the Au 4*f* spectra, and no gold oxides[127] were formed in both samples.

Hf 4*f* spectra were fitted with a fixed spin-orbit splitting of 1.67 eV, an intensity ratio of 0.75 for f-orbitals and the same FWHM for both components.[96] The spectra were aligned to the respective bulk Au $4f_{7/2}$ peaks at 84.0 eV recorded for all resistive states.

Hf $3d_{5/2}$ and Al 1s spectra for an angle of emission of 41.4° (sub-surface sensitive) and 60° (surface sensitive) were measured two and three times, respectively. The spectra corresponding to the same angle and the same memristive state were combined afterward. To this end, the single spectra were aligned to the corresponding Au $4f_{7/2}$ peak at 84.0 eV, and the backgrounds of the single spectra were subtracted before the spectra taken at one and the same angle and resistive state were summed up. Raw spectra and fitted backgrounds can be found in Section S7–S10, Supporting Information. The merged Hf $3d_{5/2}$ and Al 1s spectra could be fitted best with single Pseudo-Voigt functions.

Supporting Information

Supporting Information is available from the Wiley Online Library or from the author.

Acknowledgements

This work was funded by the Deutsche Forschungsgemeinschaft (DFG, German Research Foundation) through FOR 2093. Funded by the Deutsche Forschungsgemeinschaft (DFG, German Research Foundation)—Project-ID 434434223—SFB 1461. The authors acknowledge DESY (Hamburg, Germany), a member of the Helmholtz Association HGF, for the provision of experimental facilities. Parts of this research were carried out at PETRA III using Beamlines P04 and P22. Beamtime was allocated for proposals I-20190542, I-20190474, and I-20210450. Funding for the photoemission spectroscopy instruments at P04 and P22 by the German Federal Ministry of Education and Research (BMBF) under the framework program ErUM is gratefully acknowledged. The TEM/EELS measurements were afforded by funding from the European Union Horizon 2020 research and innovation program under grant agreement No. 823717—ESTEEM3. Further, G.K. is thankful for a fellowship from the Alexander von Humboldt foundation.

Open access funding enabled and organized by Projekt DEAL.

Conflict of Interest

The authors declare no conflict of interest.

Data Availability Statement

The data that support the findings of this study are available from the corresponding author upon reasonable request.

Keywords

analog memristive devices, electron traps, hard X-ray photoelectron spectroscopy, HfO_2, in situ photoelectron spectroscopy, memristive switching mechanisms, resistive switching

Received: November 11, 2022
Revised: February 6, 2023
Published online: April 24, 2023

[1] J. Backus, *Commun. ACM* **1978**, *21*, 613.
[2] M. Horowitz, in *2014 IEEE International Solid-State Circuits Conference Digest of Technical Papers (ISSCC)*, IEEE, Piscataway, NJ **2014**, pp. 10–14.
[3] Q. Xia, J. J. Yang, *Nat. Mater.* **2019**, *18*, 309.
[4] C. Mead, *Proc. IEEE* **1990**, *78*, 1629.
[5] I. Chakraborty, A. Jaiswal, A. K. Saha, S. K. Gupta, K. Roy, *Appl. Phys. Rev.* **2020**, *7*, 021308.
[6] J. D. Kendall, S. Kumar, *Appl. Phys. Rev.* **2020**, *7*, 011305.
[7] D. V. Christensen, R. Dittmann, B. Linares-Barranco, A. Sebastian, M. L. Gallo, A. Redaelli, S. Slesazeck, T. Mikolajick, S. Spiga, S. Menzel, I. Valov, G. Milano, C. Ricciardi, S.-J. Liang, F. Miao, M. Lanza, T. J. Quill, S. T. Keene, A. Salleo, J. Grollier, D. Marković, A. Mizrahi, P. Yao, J. J. Yang, G. Indiveri, J. P. Strachan, S. Datta, E. Vianello, A. Valentian, J. Feldmann, et al., *Neuromorph. Comput. Eng.* **2022**, *2*, 022501.
[8] G. Indiveri, S.-C. Liu, *Proc. IEEE* **2015**, *103*, 1379.

[9] E. Chicca, F. Stefanini, C. Bartolozzi, G. Indiveri, *Proc. IEEE* **2014**, *102*, 1367.
[10] G. W. Burr, R. M. Shelby, A. Sebastian, S. Kim, S. Kim, S. Sidler, K. Virwani, M. Ishii, P. Narayanan, A. Fumarola, L. L. Sanches, I. Boybat, M. Le Gallo, K. Moon, J. Woo, H. Hwang, Y. Leblebici, *Adv. Phys.: X* **2017**, *2*, 89.
[11] M. Ziegler, C. Wenger, E. Chicca, H. Kohlstedt, *J. Appl. Phys.* **2018**, *124*, 152003.
[12] M. Zhao, B. Gao, J. Tang, H. Qian, H. Wu, *Appl. Phys. Rev.* **2020**, *7*, 011301.
[13] R. Dittmann, S. Menzel, R. Waser, *Adv. Phys.* **2021**, *70*, 155.
[14] E. Chicca, G. Indiveri, *Appl. Phys. Lett.* **2020**, *116*, 120501.
[15] S. H. Jo, T. Chang, I. Ebong, B. B. Bhadviya, P. Mazumder, W. Lu, *Nano Lett.* **2010**, *10*, 1297.
[16] T. Ohno, T. Hasegawa, T. Tsuruoka, K. Terabe, J. K. Gimzewski, M. Aono, *Nat. Mater.* **2011**, *10*, 591.
[17] K. Seo, I. Kim, S. Jung, M. Jo, S. Park, J. Park, J. Shin, K. P. Biju, J. Kong, K. Lee, B. Lee, H. Hwang, *Nanotechnology* **2011**, *22*, 254023.
[18] M. Hansen, M. Ziegler, H. Kohlstedt, in *2016 IEEE International Conference on Rebooting Computing (ICRC)*, IEEE, Piscataway, NJ **2016**, pp 1–8.
[19] M. Hansen, F. Zahari, M. Ziegler, H. Kohlstedt, *Front. Neurosci.* **2017**, *11*, 1.
[20] X. Yan, Y. Pei, H. Chen, J. Zhao, Z. Zhou, H. Wang, L. Zhang, J. Wang, X. Li, C. Qin, G. Wang, Z. Xiao, Q. Zhao, K. Wang, H. Li, D. Ren, Q. Liu, H. Zhou, J. Chen, P. Zhou, *Adv. Mater.* **2019**, *31*, 1805284.
[21] X. Yan, K. Wang, J. Zhao, Z. Zhou, H. Wang, J. Wang, L. Zhang, X. Li, Z. Xiao, Q. Zhao, Y. Pei, G. Wang, C. Qin, H. Li, J. Lou, Q. Liu, P. Zhou, *Small* **2019**, *15*, 1900107.
[22] S. Park, S. Klett, T. Ivanov, A. Knauer, J. Doell, M. Ziegler, *Front. Nanotechnol.* **2021**, *3*, 16.
[23] D. B. Strukov, G. S. Snider, D. R. Stewart, R. S. Williams, *Nature* **2008**, *453*, 80.
[24] D. Ielmini, R. Waser, *Resistive Switching: From Fundamentals of Nanoionic Redox Processes to Memristive Device Applications*, Wiley-VCH, Weinheim **2016**.
[25] A. Sawa, *Mater. Today* **2008**, *11*, 28.
[26] H. Bian, Y. Y. Goh, Y. Liu, H. Ling, L. Xie, X. Liu, *Adv. Mater.* **2021**, *33*, 2006469.
[27] A. Sawa, T. Fujii, M. Kawasaki, Y. Tokura, *Appl. Phys. Lett.* **2004**, *85*, 4073.
[28] D.-j. Seong, M. Jo, D. Lee, H. Hwang, *Electrochem. Solid-State Lett.* **2007**, *10*, H168.
[29] S. Park, S. Jung, M. Siddik, M. Jo, J. Park, S. Kim, W. Lee, J. Shin, D. Lee, G. Choi, J. Woo, E. Cha, B. H. Lee, H. Hwang, *Phys. Status Solidi RRL* **2012**, *6*, 454.
[30] E. Mikheev, B. D. Hoskins, D. B. Strukov, S. Stemmer, *Nat. Commun.* **2014**, *5*, 3990.
[31] C.-W. Hsu, Y.-F. Wang, C.-C. Wan, I.-T. Wang, C.-T. Chou, W.-L. Lai, Y.-J. Lee, T.-H. Hou, *Nanotechnology* **2014**, *25*, 165202.
[32] T. You, N. Du, S. Slesazeck, T. Mikolajick, G. Li, D. Bürger, I. Skorupa, H. Stöcker, B. Abendroth, A. Beyer, K. Volz, O. G. Schmidt, H. Schmidt, *ACS Appl. Mater. Interfaces* **2014**, *6*, 19758.
[33] M. Hansen, M. Ziegler, L. Kolberg, R. Soni, S. Dirkmann, T. Mussenbrock, H. Kohlstedt, *Sci. Rep.* **2015**, *5*, 13753.
[34] Z. Fan, H. Fan, L. Yang, P. Li, Z. Lu, G. Tian, Z. Huang, Z. Li, J. Yao, Q. Luo, C. Chen, D. Chen, Z. Yan, M. Zeng, X. Lu, X. Gao, J.-M. Liu, *J. Mater. Chem. C* **2017**, *5*, 7317.
[35] N. Du, N. Manjunath, Y. Li, S. Menzel, E. Linn, R. Waser, T. You, D. Bürger, I. Skorupa, D. Walczyk, C. Walczyk, O. G. Schmidt, H. Schmidt, *Phys. Rev. Appl.* **2018**, *10*, 054025.
[36] S. Gao, G. Liu, H. Yang, C. Hu, Q. Chen, G. Gong, W. Xue, X. Yi, J. Shang, R.-W. Li, *ACS Nano* **2019**, *13*, 2634.
[37] T. D. Dongale, G. U. Kamble, D. Y. Kang, S. S. Kundale, H.-M. An, T. G. Kim, *Phys. Status Solidi* **2021**, *15*, 2100199.
[38] D. Walczyk, C. Walczyk, T. Schroeder, T. Bertaud, M. Sowińska, M. Lukosius, M. Fraschke, B. Tillack, C. Wenger, *Microelectron. Eng.* **2011**, *88*, 1133.
[39] M. K. Mahadevaiah, E. Perez, C. Wenger, A. Grossi, C. Zambelli, P. Olivo, F. Zahari, H. Kohlstedt, M. Ziegler, in *2019 IEEE International Reliability Physics Symposium (IRPS)*, IEEE, Pisataway, NJ **2019**, pp. 1–4.
[40] D. Kim, J. H. Park, D. S. Jeon, T. D. Dongale, T. G. Kim, *J. Alloys Compd.* **2021**, *854*, 157261.
[41] M. Hansen, F. Zahari, H. Kohlstedt, M. Ziegler, *Sci. Rep.* **2018**, *8*, 8914.
[42] S. Choi, Y. Kim, T. V. Nguyen, W. H. Jeong, K.-S. Min, B. J. Choi, *Adv. Electron. Mater.* **2021**, *7*, 2100050.
[43] K. M. Kim, J. Zhang, C. Graves, J. J. Yang, B. J. Choi, C. S. Hwang, Z. Li, R. S. Williams, *Nano Lett.* **2016**, *16*, 6724.
[44] Y. Yang, R. Huang, *Nat. Electron.* **2018**, *1*, 274.
[45] F. Hofer, F. P. Schmidt, W. Grogger, G. Kothleitner, *IOP Conf. Ser.: Mater. Sci. Eng.* **2016**, *109*, 012007.
[46] F. A. Stevie, C. L. Donley, *J. Vac. Sci. Technol., A* **2020**, *38*, 063204.
[47] C. Kalha, N. K. Fernando, P. Bhatt, F. O. L. Johansson, A. Lindblad, H. Rensmo, L. Z. Medina, R. Lindblad, S. Siol, L. P. H. Jeurgens, C. Cancellieri, K. Rossnagel, K. Medjanik, G. Schönhense, M. Simon, A. X. Gray, S. Nemšák, P. Lömker, C. Schlueter, A. Regoutz, *J. Phys.: Condens. Matter* **2021**, *33*, 233001.
[48] Y. Lebedinskii, A. Zenkevich, E. P. Gusev, *J. Appl. Phys.* **2007**, *101*, 074504.
[49] C. E. ViolBarbosa, C. Shekhar, B. Yan, S. Ouardi, E. Ikenaga, G. H. Fecher, C. Felser, *Phys. Rev. B* **2013**, *88*, 195128.
[50] T. Bertaud, M. Sowinska, D. Walczyk, S. Thiess, A. Gloskovskii, C. Walczyk, T. Schroeder, *Appl. Phys. Lett.* **2012**, *101*, 143501.
[51] Y. A. Matveyev, A. M. Markeev, Y. Y. Lebedinskii, A. A. Chouprik, K. V. Egorov, W. Drube, A. V. Zenkevich, *Thin Solid Films* **2014**, *563*, 20.
[52] S. U. Sharath, T. Bertaud, J. Kurian, E. Hildebrandt, C. Walczyk, P. Calka, P. Zaumseil, M. Sowinska, D. Walczyk, A. Gloskovskii, T. Schroeder, L. Alff, *Appl. Phys. Lett.* **2014**, *104*, 063502.
[53] A. S. Sokolov, Y.-R. Jeon, S. Kim, B. Ku, D. Lim, H. Han, M. G. Chae, J. Lee, B. G. Ha, C. Choi, *Appl. Surf. Sci.* **2018**, *434*, 822.
[54] G. Niu, P. Calka, P. Huang, S. U. Sharath, S. Petzold, A. Gloskovskii, K. Fröhlich, Y. Zhao, J. Kang, M. A. Schubert, F. Bärwolf, W. Ren, Z.-G. Ye, E. Perez, C. Wenger, L. Alff, T. Schroeder, *Mater. Res. Lett.* **2019**, *7*, 117.
[55] C. Baeumer, T. Heisig, B. Arndt, K. Skaja, F. Borgatti, F. Offi, F. Motti, G. Panaccione, R. Waser, S. Menzel, R. Dittmann, *Faraday Discuss.* **2019**, *213*, 215.
[56] J. H. Yoon, S. J. Song, I.-H. Yoo, J. Y. Seok, K. J. Yoon, D. E. Kwon, T. H. Park, C. S. Hwang, *Adv. Funct. Mater.* **2014**, *24*, 5086.
[57] C. Baeumer, C. Schmitz, A. H. H. Ramadan, H. Du, K. Skaja, V. Feyer, P. Müller, B. Arndt, C.-L. Jia, J. Mayer, R. A. De Souza, C. Michael Schneider, R. Waser, R. Dittmann, *Nat. Commun.* **2015**, *6*, 8610.
[58] S. Stathopoulos, A. Khiat, M. Trapatseli, S. Cortese, A. Serb, I. Valov, T. Prodromakis, *Sci. Rep.* **2017**, *7*, 17532.
[59] A. Hardtdegen, C. L. Torre, F. Cüppers, S. Menzel, R. Waser, S. Hoffmann-Eifert, *IEEE Trans. Electron Devices* **2018**, *65*, 3229.
[60] J. H. Lee, J. H. Park, T. D. Dongale, T. G. Kim, *J. Alloys Compd.* **2020**, *821*, 153247.
[61] J. H. Sung, J. H. Park, D. S. Jeon, D. Kim, M. J. Yu, A. C. Khot, T. D. Dongale, T. G. Kim, *Mater. Des.* **2021**, *207*, 109845.

[62] Q. Wang, Y. Wang, R. Luo, J. Wang, L. Ji, Z. Jiang, C. Wenger, Z. Song, S. Song, W. Ren, J. Bi, G. Niu, *Neuromorph. Comput. Eng.* **2022**, *2*, 044012.
[63] Y. Kim, Y. J. Kwon, D. E. Kwon, K. J. Yoon, J. H. Yoon, S. Yoo, H. J. Kim, T. H. Park, J.-W. Han, K. M. Kim, C. S. Hwang, *Adv. Mater.* **2018**, *30*, 1704320.
[64] J. Robertson, R. M. Wallace, *Mater. Sci. Eng.: R: Rep.* **2015**, *88*, 1.
[65] H. H. Radamson, H. Zhu, Z. Wu, X. He, H. Lin, J. Liu, J. Xiang, Z. Kong, W. Xiong, J. Li, H. Cui, J. Gao, H. Yang, Y. Du, B. Xu, B. Li, X. Zhao, J. Yu, Y. Dong, G. Wang, *Nanomaterials* **2020**, *10*, 1555.
[66] H.-W. You, W.-J. Cho, *Appl. Phys. Lett.* **2010**, *96*, 093506.
[67] D. Bach, R. Schneider, D. Gerthsen, J. Verbeeck, W. Sigle, *Microsc. Microanal.* **2009**, *15*, 505.
[68] C. Nico, T. Monteiro, M. Graça, *Prog. Mater. Sci.* **2016**, *80*, 1.
[69] S. Sze, K. K. Ng, *Phys. Semicond. Devices*, Wiley, Hoboken, NJ **2006**.
[70] M. S. Tyagi, in *Metal-Semiconductor Schottky Barrier Junctions and Their Applications* (Ed: B. L. Sharma), Springer US, Boston, MA **1984**, pp. 1–60.
[71] S. Dirkmann, M. Hansen, M. Ziegler, H. Kohlstedt, T. Mussenbrock, *Sci. Rep.* **2016**, *6*, 35686.
[72] S. Yarragolla, T. Hemke, J. Trieschmann, F. Zahari, H. Kohlstedt, T. Mussenbrock, *J. Appl. Phys.* **2022**, *131*, 134304.
[73] E. Barsoukov, J. R. Macdonald, editors, *Impedance Spectroscopy: Theory, Experiment, and Applications*, 3rd Edition, Wiley, Hoboken, NJ, USA **2018**.
[74] R. Marquardt, F. Zahari, J. Carstensen, G. Popkirov, O. Gronenberg, G. Kolhatkar, H. Kohlstedt, M. Ziegler, *Adv. Electron. Mater*, https://doi.org/10.1002/aelm.202201227.
[75] S. Zafar, A. Callegari, E. Gusev, M. V. Fischetti, *J. Appl. Phys.* **2003**, *93*, 9298.
[76] H. Schroeder, V. V. Zhirnov, R. K. Cavin, R. Waser, *J. Appl. Phys.* **2010**, *107*, 054517.
[77] S.-O. Park, H. Jeong, J. Park, J. Bae, S. Choi, *Nat. Commun.* **2022**, *13*, 2888.
[78] S. Ambrogio, P. Narayanan, H. Tsai, R. M. Shelby, I. Boybat, C. di Nolfo, S. Sidler, M. Giordano, M. Bodini, N. C. P. Farinha, B. Killeen, C. Cheng, Y. Jaoudi, G. W. Burr, *Nature* **2018**, *558*, 60.
[79] E. A. Cartier, W. Kim, N. Gong, T. Gokmen, M. M. Frank, D. M. Bishop, Y. Kim, S. Kim, T. Ando, E. Y. Wu, P. Adusumilli, J. Rozen, P. M. Solomon, W. Haensch, M. J. BrightSky, A. Sebastian, G. W. Burr, V. Narayanan, in *2019 IEEE International Reliability Physics Symposium (IRPS)*, IEEE, Piscataway **2019**, pp. 1–10.
[80] J. Strobel, M. Hansen, S. Dirkmann, K. K. Neelisetty, M. Ziegler, G. Haberfehlner, R. Popescu, G. Kothleitner, V. S. K. Chakravadhanula, C. Kübel, H. Kohlstedt, T. Mussenbrock, L. Kienle, *J. Appl. Phys.* **2017**, *121*, 245307.
[81] S. U. Sharath, S. Vogel, L. Molina-Luna, E. Hildebrandt, C. Wenger, J. Kurian, M. Duerrschnabel, T. Niermann, G. Niu, P. Calka, M. Lehmann, H.-J. Kleebe, T. Schroeder, L. Alff, *Adv. Funct. Mater.* **2017**, *27*, 1700432.
[82] S. Fritz, A. Seiler, L. Radtke, R. Schneider, M. Weides, G. Weiß, D. Gerthsen, *Sci. Rep.* **2018**, *8*, 1.
[83] J. H. Jang, H.-S. Jung, J. H. Kim, S. Y. Lee, C. S. Hwang, M. Kim, *J. Appl. Phys.* **2011**, *109*, 023718.
[84] D. Bouchet, C. Colliex, *Ultramicroscopy* **2003**, *96*, 139.
[85] T. Imamura, S. Hasuo, *Appl. Phys. Lett.* **1991**, *58*, 645.
[86] X. Kang, L. Ying, H. Wang, G. Zhang, W. Peng, X. Kong, X. Xie, Z. Wang, *Phys. C* **2014**, *503*, 29.
[87] N. Jiang, J. C. H. Spence, *Ultramicroscopy* **2006**, *106*, 215.
[88] H. O. Ayoola, C.-H. Li, S. D. House, C. S. Bonifacio, K. Kisslinger, J. Jinschek, W. A. Saidi, J. C. Yang, *Ultramicroscopy* **2020**, *219*, 113127.
[89] C. Guedj, L. Hung, A. Zobelli, P. Blaise, F. Sottile, V. Olevano, *Appl. Phys. Lett.* **2014**, *105*, 222904.
[90] C. Li, Y. Yao, X. Shen, Y. Wang, J. Li, C. Gu, R. Yu, Q. Liu, M. Liu, *Nano Res.* **2015**, *8*, 3571.
[91] K. Lee, K. Park, H.-J. Lee, M. S. Song, K. C. Lee, J. Namkung, J. H. Lee, J. Park, S. C. Chae, *Sci. Rep.* **2021**, *11*, 6290.
[92] J. Viefhaus, F. Scholz, S. Deinert, L. Glaser, M. Ilchen, J. Seltmann, P. Walter, F. Siewert, *Nucl. Instrum. Methods Phys. Res., Sect. A* **2013**, *710*, 151.
[93] C. Schlueter, A. Gloskovskii, K. Ederer, I. Schostak, S. Piec, I. Sarkar, Y. Matveyev, P. Lömker, M. Sing, R. Claessen, C. Wiemann, C. M. Schneider, K. Medjanik, G. Schönhense, P. Amann, A. Nilsson, W. Drube, *AIP Conf. Proc.* **2019**, *2054*, 040010.
[94] S. Tanuma, C. J. Powell, D. R. Penn, *Surf. Interface Anal.* **2011**, *43*, 689.
[95] C. J. Powell, *J. Vac. Sci. Technol., A* **2020**, *38*, 023209.
[96] C. Morant, L. Galán, J. M. Sanz, *Surf. Interface Anal.* **1990**, *16*, 304.
[97] V. Kruchinin, V. Aliev, T. Perevalov, D. Islamov, V. Gritsenko, I. Prosvirin, C. Cheng, A. Chin, *Microelectron. Eng.* **2015**, *147*, 165.
[98] S. Kim, S. Woo, H. Kim, I. Kim, K. Lee, W. Jeong, T. P. a. H. Jeon, *J. Korean Phys. Soc.* **2008**, *52*, 1103.
[99] Y. Matveyev, A. Zenkevich, Y. Lebedinskii, S. Thiess, W. Drube, *Microelectron. Eng.* **2011**, *88*, 1353.
[100] Y. Abe, N. Miyata, E. Ikenaga, H. Suzuki, K. Kitamura, S. Igarashi, H. Nohira, *Jpn. J. Appl. Phys.* **2009**, *48*, 041201.
[101] T. Szyjka, L. Baumgarten, T. Mittmann, Y. Matveyev, C. Schlueter, T. Mikolajick, U. Schroeder, M. Müller, *ACS Appl. Electron. Mater.* **2020**.
[102] C. Künneth, R. Batra, G. A. Rossetti, R. Ramprasad, A. Kersch, in *Ferroelectricity in Doped Hafnium Oxide: Materials, Properties and Devices*, Elsevier, New York **2019**, pp. 245–289.
[103] A. G. Shard, *J. Vac. Sci. Technol., A* **2020**, *38*, 041201.
[104] E. Kröger, A. Petraru, A. Quer, R. Soni, M. Kalläne, N. A. Pertsev, H. Kohlstedt, K. Rossnagel, *Phys. Rev. B* **2016**, *93*, 235415.
[105] Y. Matveyev, D. Negrov, A. Chernikova, Y. Lebedinskii, R. Kirtaev, S. Zarubin, E. Suvorova, A. Gloskovskii, A. Zenkevich, *ACS Appl. Mater. Interfaces* **2017**, *9*, 43370.
[106] M. K. Mendes, E. Martinez, J. M. Ablett, M. Veillerot, R. Gassilloud, M. Bernard, O. Renault, J. P. Rueff, N. Barrett, *Sci. Rep.* **2018**, *8*, 1.
[107] V. Solokha, T.-L. Lee, A. Wilson, K. Hingerl, J. Zegenhagen, *J. Electron Spectrosc. Relat. Phenom.* **2018**, *225*, 28.
[108] A. Beni, N. Ott, M. Pawelkiewicz, M. Wardé, K. Young, B. Bauer, P. Rajput, B. Detlefs, J. Zegenhagen, R. McGrath, M.-G. Barthés-Labrousse, L. P. H. Jeurgens, P. Schmutz, *Electrochem. Commun.* **2014**, *46*, 13.
[109] A. Shetty, B. Roul, S. Mukundan, L. Mohan, G. Chandan, K. J. Vinoy, S. B. Krupanidhi, *AIP Adv.* **2015**, *5*, 097103.
[110] S. Petzold, E. Miranda, S. U. Sharath, J. Muñoz-Gorriz, T. Vogel, E. Piros, N. Kaiser, R. Eilhardt, A. Zintler, L. Molina-Luna, J. Suñé, L. Alff, *J. Appl. Phys.* **2019**, *125*, 234503.
[111] P. Broqvist, A. Pasquarello, *Appl. Phys. Lett.* **2006**, *89*, 262904.
[112] H. Kawano, *Prog. Surf. Sci.* **2022**, *97*, 100583.
[113] X. Wang, K. Han, W. Wang, X. Ma, D. Chen, J. Zhang, J. Du, Y. Xiong, A. Huang, *Appl. Phys. Lett.* **2010**, *97*, 062901.
[114] A. Winzer, N. Szabó, J. Ocker, R. Hentschel, M. Schuster, F. Schubert, J. Gärtner, A. Wachowiak, T. Mikolajick, *J. Appl. Phys.* **2015**, *118*, 124106.
[115] K. P. McKenna, *Modelling Simul. Mater. Sci. Eng.* **2014**, *22*, 025001.
[116] X. Wang, K. Han, W. Wang, J. Xiang, H. Yang, J. Zhang, X. Ma, C. Zhao, D. Chen, T. Ye, *Appl. Phys. Lett.* **2012**, *100*, 122907.
[117] T. Grasser, *Microelectron. Reliab.* **2012**, *52*, 39.
[118] C. Lenser, A. Köhl, M. Patt, C. M. Schneider, R. Waser, R. Dittmann, *Phys. Rev. B* **2014**, *90*, 115312.
[119] A. de Sa, C. Rangel, P. Skeldon, G. Thompson, *Port. Electrochim. Acta* **2006**, *24*, 305.

[120] A. J. Bard, L. R. Faulkner, *Electrochem. Methods: Fundam. Appl.*, 2nd edition, Wiley, New York **2001**.
[121] F. Zahari, F. Schlichting, J. Strobel, S. Dirkmann, J. Cipo, S. Gauter, J. Trieschmann, R. Marquardt, G. Haberfehlner, G. Kothleitner, L. Kienle, T. Mussenbrock, M. Ziegler, H. Kersten, H. Kohlstedt, *J. Vac. Sci. Technol., B* **2019**, *37*, 061203.
[122] J.-Y. Kwon, T.-S. Yoon, K.-B. Kim, S.-H. Min, *J. Appl. Phys.* **2003**, *93*, 3270.
[123] M. Schmid, H.-P. Steinrück, J. M. Gottfried, *Surf. Interface Anal.* **2014**, *46*, 505.
[124] D. A. Shirley, *Phys. Rev. B* **1972**, *5*, 4709.
[125] J. Leiro, E. Minni, E. Suoninen, *J. Phys. F: Met. Phys.* **1983**, *13*, 215.
[126] P. H. Citrin, G. K. Wertheim, Y. Baer, *Phys. Rev. Lett.* **1978**, *41*, 1425.
[127] H. Tsai, E. Hu, K. Perng, M. Chen, J.-C. Wu, Y.-S. Chang, *Surf. Sci.* **2003**, *537*, L447.